

Copyright
by
Sanghoon Oh
2006

**The Dissertation Committee for Sanghoon Oh Certifies that this is the approved
version of the following dissertation:**

Dispersion in Biomedical Optical Imaging Systems

Committee:

Thomas E. Milner, Supervisor

H. Grady Rylander III

Baxter Womack

Michael Becker

Massoud Motamedi

Dispersion in Biomedical Optical Imaging Systems

by

Sanghoon Oh, B.S.; M.S.E.

Dissertation

Presented to the Faculty of the Graduate School of

The University of Texas at Austin

in Partial Fulfillment

of the Requirements

for the Degree of

Doctor of Philosophy

The University of Texas at Austin

May 2006

Dedication

To my family:

Wife Mijung, Daughter Suah,Minah
Father Jemmo Oh, Mother Soonhyung Choi,
and Brother Minyoung Oh.

Acknowledgements

There are numerous people whom I would like to thank for helping me to finish my graduate life. First of all, I would like to express my special appreciation to my supervisor, Dr. Thomas E. Milner, for guiding and training me as a research scholar. I thank him also for his patient and gracious research help. He has shared not only his innovative research ideas but also Christian faith to encourage me to have a peaceful mind. I have had a really long journey of Ph.D. work to reach my goal, and he has been the man who points the most righteous direction to the next destination. Many thank to Dr. Michael Becker and Dr. Baxter Womack for giving me many opportunities to have a teaching assistantship of EE464 and for always treating me as a member of their families; they have been my best teaching mentors. I thank particularly Dr. H Grady Rylander III and Dr. Massoud Motamedi for sharing valuable ideas and discussions. I want to show gratitude to Mrs. Vicki Stratton for her supporting work including her expertise in administration; she has been a skillful nanny of the biomedical optics laboratory. I want to thank Dr. Rebecca Richards-Kortum for initiating my interest in biophotonics research and providing support for my Masters Degree work.

It would have been impossible to finish my Ph.D. work without collaborations of lab members and friends; Chris, Nate, Jesung, Roberto, Jordan, Junghwan, Jihoon, Wook, Bo, Jaesook, Gracy, Jeehyun, Hoya, and Eunha. I have had valuable discussions with

them and gotten instant feedbacks from them. They have afforded critical suggestions based on their practical and professional experiences. Moreover, I have had plenty of joyful time with them.

I thank my neighbors and church members for their friendship and prayer for me and my family.

I would like to thank my father, mother, grand mother, and brother for their devoted love and endless mental support. 아버지 어머니 박사 마칠 수 있도록 잘 성장하게 해 주심에 정말 감사합니다. Also, there are two precious ladies to thank, my daughters Suah and Minah who make me smile happily at all times. In addition, I would like to extend my special thanks to my wife, Mijung, for her heartfelt love and support. She is the suitable helper of my life, and I will never forget her help and prayer throughout my entire life, which makes me a good daddy of adorable daughters and a righteous man in our societies.

Dispersion in Biomedical Optical Imaging Systems

Publication No. _____

Sanghoon Oh, Ph.D.

The University of Texas at Austin, 2006

Supervisor: Thomas E. Milner

Dispersion caused by the refractive index variation over a spectral range is an important characteristic to identify the structure and composition of materials. This research reports on work to obtain dispersion information using both time and spectral domain optical coherence tomography. To process time-frequency data, a non-uniform Fourier transformation is applied to remove the resolved non-uniform frequency sampling. Analysis of the spectral phase function in the optical frequency domain is applied to measure the dispersion. First, this research experimented with water (H₂O) to measure dispersion. The measured dispersion of water is compared with known data to confirm the methodology. Second, the concentration of a glucose solution was estimated by analyzing the spectral phase function. The result showed that this method can provide an ability to measure glucose concentration with high sensitivity 0.54 mM. In conclusion, this method can be implemented to monitor sample constituents and to compensate for material dispersion.

Table of Contents

LIST OF FIGURES	xi
CHAPTER 1: INTRODUCTION.....	1
1.1. Background and Motivation.....	1
1.1.1. Optical Imaging.....	1
1.1.2. Dispersion.....	4
1.2. Dissertation Overview	5
1.3. References	7
CHAPTER 2: DISPERSION CONTROL SYSTEM FOR OPTICAL COHERENCE TOMOGRAPHY: FEASIBILITY STUDY	9
2.1. Abstract	9
2.2. Introduction	11
2.3. Methods.....	12
2.3.1. Simulations.....	12
2.3.1.1. Computing group delay	12
2.3.1.2. Numerical Calculation of Coherence Function affected by Dispersion.....	14
2.3.2. Experiment	16
2.3.2.1. Dispersion Controller.....	16
2.3.2.2. Experimental Setup.....	17
2.3.2.3. Measurement of Group Delay caused by Water.....	19
2.4. Results	21
2.5. Discussion	24
2.6. Conclusion.....	25
2.7. References	26
CHAPTER 3: METHOD TO CALIBRATE SPATIAL LIGHT MODULATOR (SLM) USING DIFFERENTIAL PHASE OPTICAL COHERENCE TOMOGRAPHY (DPOCT)	27
3.1. Introduction	27

3.2. Methods	29
3.2.1. Experimental System.....	29
3.2.2. Spatial Light Modulator (SLM).....	34
3.2.3. Differential Phase Optical Coherence Tomography (DPOCT).....	36
3.2.4. Experimental Procedure	39
3.3. Results	41
3.4. Discussion	43
3.5. Conclusion.....	45
3.6. References	46
CHAPTER 4: A FIBER-BASED COMMON-PATH SPECTRAL INTERFEROMETER FOR MEASUREMENT OF HIGHER-ORDER REFRACTIVE INDEX AND DISPERSION	48
4.1. Introduction	48
4.2. Methodology	51
4.2.1. Spectral Phase Analysis.....	51
4.2.2. Experimental System.....	55
4.2.2.1. Measurement of Dispersion.....	55
4.2.2.2. Measurement of Glucose Concentration	57
4.2.3. Data Processing	59
4.2.3.1. Non-Uniform Fourier Transformation.....	59
4.2.3.2. Multitaper Spectral Analysis	61
4.2.3.3. Spectral Interference Analysis.....	63
4.2.3.4. Optical Path Length Estimation.....	67
4.3. Results	70
4.4. Discussion	77
4.5. Conclusion.....	79
4.6. References	81
CHAPTER 5: SUMMARY AND CONCLUSIONS	86
5.1. Summary of Dissertation.....	86
5.2. Conclusions	88

CHAPTER 6: FUTURE WORK – OPTICAL IMAGING AND CHARACTERIZATION OF CANCER CELLS USING SPECTRAL DOMAIN OPTICAL COHERENCE TOMOGRAPHY FOR EARLY CANCER DIAGNOSIS.	89
6.1. Introduction	89
6.2. Methods	91
6.2.1. The First Mode: Spatially Multiplexed Swept Source Optical Coherence Tomography	91
6.2.2. The second mode: Spectroscopic Optical Coherence Tomography	96
6.3. Expected Results and Discussion.....	100
6.4. References	102
GLOSSARY.....	104
BIBLIOGRAPHY.....	106
VITA	116

List of Figures

Figure 1.1. An illustration of time-domain OCT system	2
Figure 2.1. Procedures to compute group delay	13
Figure 2.2. Refractive index of water; real part (upper) and imaginary part (lower).....	15
Figure 2.3. Diagram of dispersion controller.....	16
Figure 2.4. Optical experimental setup; interferometer with dispersion controller. Red dotted line: sample path, blue dotted line: reference path.....	18
Figure 2.5. Block diagram of dispersion control system	19
Figure 2.6. (a) top: phase data of dispersed and non-dispersed coherence function in frequency domain, (b) middle: phase shift is difference between the two data in (a), and (c) bottom: wrapped phase shift data for SLM.....	21
Figure 2.7. A graph of phase shift variation versus sample depth from simulation result.....	22
Figure 2.8. Phase shift versus wavelength (experimental data).....	23
Figure 3.1. Experimental system; L: lens, M: mirror, M-G: mirror mounted on Galvanometer, G: grating, C: collimator with FC/APC optical connector, W: Wollaston Prism, D: photodetector, Seg: segment, ADC: analog to digital converter, RSDL: rapid scanning delay line, small squares and numbers above represent spliced locations and angles.	30
Figure 3.2. A detailed view of sample path with light trace; L: Triplet lens, W: Wollaston prism, OL: microscope objective lens, E: extraordinary axis, O: ordinary axis, f: focal length of the triplet lens, θ : diverged angle (2°), 4-f geometry with two lenses and two Wollaston prisms	31
Figure 3.3. SLM consists of a controller and a liquid crystal window.	34

Figure 3.4. A graph of the electro-optical response of the SLM liquid crystal. Data is a double pass, mean of 10 liquid crystal cells. Range of levels (0 to 4095) with respect to electric input voltage (0 to 10 V).....	42
Figure 3.5. Standard deviation of 10 liquid crystal cells.	44
Figure 4.1. Fiber-based common-path spectral interferometer using a frequency swept laser source. 1, 2, and 3: port number, C: collimator, R: reference plate, WC: a water filled sample chamber.	55
Figure 4.2. Experimental system: common-path spectral interferometer. C: collimator, L: plano-convex lens, SC: sample chamber, and ADC: analog-to-digital converter.....	57
Figure 4.3. Interference fringes in path length difference domain. Sample path layout is given in inserted box. 1, 2, A, B, C, and D are labels for each surface. 2/A, 2/B, 2/C, and 2/D are labels for interference fringes corresponding to mixing of reflections from the two surfaces. Incident light propagates from left to right.	64
Figure 4.4. Detailed diagram of interferometer sample path. $\varphi_{\alpha}(\nu)$ and $\varphi_{\beta}(\nu)$ represent the spectral phase functions of 2/C and 2/B interference fringes, respectively. l_a , l_g , and l_s are physical path length in air, glass, and water; n_a , n_g , and n_s are refractive indices of air, glass, and water, respectively. The blue lines indicate light input while red are reflected light.	66
Figure 4.5. Detailed diagram of interferometer sample path. $\varphi_{1/C}(\nu)$ and $\varphi_{1/B}(\nu)$ represent the spectral phase functions generated from 1/C and 1/B interference fringes, respectively. l_r , l_a , l_g , and l_s are physical path lengths in lens, air, glass, and sample; n_r , n_a , n_g , and n_s are refractive indices of lens, air, glass, and sample, respectively. Thick blue lines indicate light input while red thin lines are reflected light.	67
Figure 4.6. Interference fringe intensity versus optical path length computed from Lomb-Scargle periodogram analysis. This data provides the depth-scanned information of the optical construction of the sample chamber.....	68

Figure 4.7. Experimentally measured spectral phase variation. Mean of 20 experimental measurements (solid) and 5th order polynomial curve fitting of the mean (dashed).	71
Figure 4.8. Spectral phase variation of refractive index of water estimated by numerical calculation using published water refractive index (solid), 5th order polynomial curve fitting (dashed).	72
Figure 4.9. Comparison of the two results; 5th order polynomial curve fits of experimental result (dashed) and numerical calculation (solid). Correlation coefficient = 0.995, Normalized mean square error = 0.002.....	73
Figure 4.10. Glucose concentration measurement for 0-5 mM in 1 mM increments (a) and 0-50 mM in 5 mM increments (b). Each error-bar represents the standard deviation of 20 measurements.....	75
Figure 6.1. Illustration of SMSS-OCT principle: multiplexing excessively long depth scan (a) into a laterally adjacent B-scans (b). L : maximum scan depth, ΔL : longitudinal resolution, Δd : lateral resolution, a : scan depth, d : lateral scan range.....	92
Figure 6.2. System diagram of SMSS-OCT imaging system. BS: beam splitter, C: collimator, M: mirror, M-G: mirror on the galvanometer, L: lens, and ADC: analog to digital converter.....	93
Figure 6.3. SMSS-OCT image of microscope cover slide; glass, 100 μ m thickness, $n=1.5$	94
Figure 6.4. Second mode; spectroscopic OCT. C: collimator, R: reference glass plate, M-G: mirror on the galvanometer, L: lens, and ADC: analog to digital converter.	96
Figure 6.5. High-order spectral phase variation of water (H ₂ O).....	97

Chapter 1: Introduction

1.1. BACKGROUND AND MOTIVATION

1.1.1. Optical Imaging

Biophotonics is rapidly developing and widely utilized in biological and medical research. Optical imaging and optical spectroscopy are two major research areas. Optical coherence tomography (OCT) was introduced by James Fujimoto in 1991 and is a highly sensitive interferometric method measuring light reflection from a target sample ^[1.1]. OCT is a promising modality to improve the quality of biomedical imaging ^[1.2, 1.3]. Development of spectrally broad-band laser sources has pushed OCT resolution to a few micrometers that is sufficient to resolve and image cross-sectional subcellular structures of tissue samples in vivo.

In terms of measurement domains, OCT can be categorized into two types; time-domain and spectral domain OCT. Time-domain OCT was introduced first and requires a mechanically moving component for changing the optical path length of light in a reference path in order to process a depth scan. Spectral domain OCT was introduced later and does not require mechanical scanning. Spectral-domain OCT needs either a frequency swept laser source or a spectrometer in the detection path of the interferometer.

According to reported research, spectral domain OCT provides better sensitivity of up to 30 dB over time domain OCT^[1,4-1,6]. Figure 1.1 illustrates basic layout of a time-domain OCT system. The system consists of a Michelson type interferometer and utilizes a broadband light source, a beam splitter, a reference reflector, a sample, and a photodetector. The broadband laser source enters the interferometer, and light is split into reference and the sample paths by the beam splitter. Light reflected from the both paths recombine at the beam splitter and interfere. Half of the interfering light is detected at the photodetector. Detected photon number spectral density (n_D) at the photodetector is

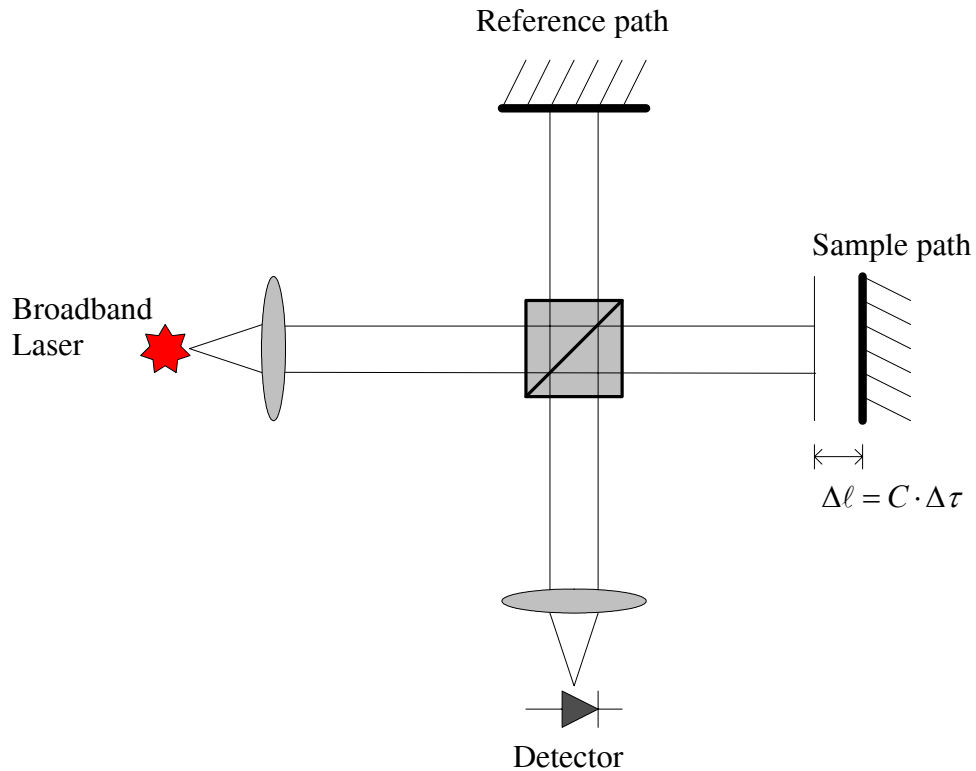


Figure 1.1. An illustration of time-domain OCT system

$$n_D = \eta |a_0(\nu)| \left[|s|^2 + |r|^2 + 2|s||r| \cos\left(\frac{4\pi\nu\Delta\ell}{C} + (\phi_s - \phi_r)\right) \right] \quad (1.1)$$

where, η is quantum efficiency of the photodetector,

$|a_0(\nu)|$ is photon number spectral density of the broadband light source,

ν is optical frequency

s is sample path reflectivity,

r is reference path reflectivity,

$\Delta\ell$ is optical path length difference between reference and sample paths,

ϕ_s is phase off-set of the sample path, and

ϕ_r is phase off-set of the reference path.

In time domain OCT, measured fringe data is a function of optical path length difference ($\Delta\ell$) associated with $\Delta\tau$. In spectral-domain OCT, fringe data is measured with respect to optical frequency (ν). Measured data from either approach can be transferred to the other domain through a time-frequency transformation (e.g. FFT). An issue in time- and spectral-domain OCT is use of broadband laser sources that introduce dispersion.

1.1.2. Dispersion

Dispersion is the physical phenomenon whereby the phase velocity of a wave depends on its temporal frequency ^[1.7,1.8]. The wider spectral range of laser source, the more dispersion becomes an issue to image a dispersive sample. Dispersion can degrade information in optical images. For example, resolution of an OCT imaging system is reduced by increasing the coherence length, producing an asymmetrical coherence function, and blurring acquired images ^[1.9,1.10]. Thus it is important to minimally be aware of dispersion effects in the optical imaging system and possibly correct for improved images. Numerous research results have been reported to demonstrate methods of dispersion calculation ^[1.8,1.11-1.14] and dispersion compensation ^[1.9,1.10,1.15,1.16] using either a mathematical approach or adding optical components to the imaging system.

Although dispersion is often viewed as problematic in optical imaging an alternative viewpoint is its measurement can be utilized to characterize materials similar to conventional absorption and transmission spectroscopy. Dispersion information can be useful to identify a dispersive material or the constituents. A motivation of this dissertation is to measure dispersion in a target material and identify the material by measurements recorded with an OCT system.

Contributions of this dissertation include introduction and verification of a new optical imaging system and data analysis for dispersion measurement and material identification. Work reported improves optical technologies to provide a more sensitive and accurate measurement tool for various areas of medical and biological research.

1.2. DISSERTATION OVERVIEW

The motivation of this dissertation is to demonstrate measurement and use of dispersion information. In this dissertation, we demonstrate optical measurement systems in the time- and spectral-domain. Also a novel data processing procedure is introduced to estimate high-order refractive index of a dispersive material.

Chapter 2 describes a dispersion control system in a time domain OCT system. The system includes a unique configuration of a Michelson interferometer, a spatial light modulator (SLM) in a 4-f geometry. Deionized ultra high filtered water (DIUF) is used as a dispersive target material. This chapter presents a feasibility test of the system, and the experimental results are verified with mathematical simulation. Comparison of the experimental and simulation results demonstrates good agreement.

Chapter 3 introduces a new method to calibrate an SLM by use of differential phase OCT^[1,17]. As the major control part of the dispersion control system, the SLM must be calibrated and its phase response function for light modulation should be estimated for design of the control system. Differential phase OCT has 0.05 rad (~5 nm) accuracy and incorporates a dual-channel interferometer that cancels common-mode phase noise.

Chapter 4 describes dispersion measurement for material identification. The measurement system is a spectral interferometer that is analogous to spectral domain OCT, and the target material is DIUF water. The spectral interferometry system includes a spectrally broadband swept laser and a fiber based common-path interferometer. Acquired fringe data is processed with a novel procedure to analyze spectral phase variation including dispersion information. Chapter 4 also includes quantitative

measurement of glucose concentration in an aqueous solution. This method demonstrates a highly accurate and stable technique to monitor glucose by a convenient measurement.

Chapter 5 reviews each chapter and summaries the research described in this dissertation. Chapter 6 provides direction for future research.

1.3. REFERENCES

- [1.1] Huang D, Swanson EA, Lin CP, Schuman JS, Stinson WG, Chang W, Hee MR, Flotte T, Gregory K, Puliafito CA, and Fujimoto JG, Optical coherence tomography, *Science*, **254**(5035), 1178-1181, 1991.
- [1.2] Fercher AF, Drexler W, Hitzenberger CK and Lasser T, Optical coherence tomography—principles and applications, *Reports on Progress in Physics*, **66**, [239-303](#), 2003.
- [1.3] Schmitt JM, Optical Coherence Tomography (OCT): A Review, *IEEE Journal of Selected Topics in Quantum Electronics*, **5**(4), 1205-1215, 1999.
- [1.4] Choma MA, Sarunic MV, Yang C, and Izatt JA, Sensitivity advantage of swept source and Fourier domain optical coherence tomography, *Optics Express*, **11**, 2183-2189, 2003.
- [1.5] DeBoer JF, Cense B, Park BH, Pierce MC, Tearney GJ, and Bouma BE, Improved signal-to-noise ratio in spectral-domain compared with time-domain optical coherence tomography, *Optics Letters*, **28**, 2067-2069, 2003.
- [1.6] Leitgeb R, Hitzenberger CK, and Fercher AF, Performance of Fourier domain vs. time domain optical coherence tomography, *Optics Express*, **11**, 889-894, 2003.
- [1.7] Born M and Wolf E, *Principal of optics 7th ed.*, p.14-24, Cambridge University Press, Cambridge, 1999.
- [1.8] Walmsley I, Waxer L, Dorrer C, The role of dispersion in ultrafast optics, *Review of Scientific Instruments*, **72**(1), 1-29, 2001.
- [1.9] Wojtkowski M, Srinivasan VJ, Ko TH, Fujimoto JG, Kowalczyk A, and Duker JS, Ultrahigh-resolution, high-speed, Fourier domain optical coherence tomography and methods for dispersion compensation, *Optics Express*, **12**(11), 2404-2422, 2004.
- [1.10] Marks DL, Oldenburg AL, Reynolds JJ, and Boppart SA, Autofocus algorithm for dispersion correction in optical coherence tomography, *Applied Optics*, **42**(16), 3038-3046, 2003.
- [1.11] Kim YL, Walsh JT Jr., and Glucksberg M.R, Phase-slope and group-dispersion calculations in the frequency domain by simple optical low-coherence reflectometry, *Applied Optics*, **42**(34), 6959-6966, 2003.

- [1.12] Hammer DX, Welch AJ, Noojin GD, Thomas RJ, Stolarski DJ, and Rockwell BA, Spectrally resolved white-light interferometry for measurement of ocular dispersion, *Journal of Optical Society of America A*, **16**(9), 2092-2102, 1999.
- [1.13] Hitzenberger CK, Baumgartner A, Drexler W, and Fercher AF, Dispersion effects in partial coherence interferometry: Implications for intraocular ranging, *Journal of Biomedical Optics*, **4**(1), 144-151, 1999.
- [1.14] Knox WH, Pearson NM, Li KD, and Hirlimannt CA, Interferometric measurements of femtosecond group delay in optical components, *Optics Letters*, **13**(7), 574-576, 1988.
- [1.15] Fercher AF, Hitzenberger CK, Sticker M, Zawadzki R, Karamata B, and Lasser T, Dispersion compensation for optical coherence tomography depth-scan signals by a numerical technique, *Optics Communications*, **204**, 67-74, 2002.
- [1.16] Fercher AF, Hitzenberger CK, Sticker M, Zawadzki R, Karamata B, and Lasser T, Numerical dispersion compensation for Partial Coherence Interferometry and Optical Coherence Tomography, *Optics Express*, **9**(12), 610-615, 2001.
- [1.17] Dave DP and Milner TE, Optical low-coherence reflectometer for differential phase measurement, *Optics Letters*, **25**(4), 227-229, 2000.

Chapter 2: Dispersion Control System for Optical Coherence Tomography: Feasibility Study

2.1. ABSTRACT

Chromatic dispersion arises when wave phase velocity depends on frequency (ν) or wavelength (λ) ^[2.1] and can pose a problem in optical biomedical imaging instrumentation ^[2.2]. Optical imaging instrumentation such as optical coherence tomography (OCT) frequently use broadband light sources to obtain better images ^[2.3]. Recorded images from instruments that use a broadband light source can be degraded since the refractive index and phase of scattered light amplitude is not constant but varies with wavelength ^[2.1]. In many imaging applications, control of dispersion is useful to obtain accurate imaging information. This study reports on a dispersion control system which varies the phase delay of each wavelength. The dispersion control system is composed of a spatial light modulator (SLM), two lenses, and two gratings configured in a 4-f geometry. To test feasibility of the system, we have computed the dispersion and evaluated group delay from measured data, and then find the phase shift function to input into the dispersion control system.

We conclude that dispersion in an optical imaging system can be determined by phase analysis of the coherence function in the frequency domain. Amount of dispersion

increases linearly with sample path length. The system introduced can measure group delay and generate a dispersion compensating function for the SLM.

2.2. INTRODUCTION

Optical imaging technologies have developed rapidly over last two decades. Some technologies are excellent imaging modalities for medical diagnosis and biological research ^[2.4-2.7]. Optical technologies are emerging as the next generation in medical imaging, in addition to X-ray, ultrasonic, and magnetic resonance imaging. Optical coherence tomography (OCT) is one optical imaging technology that has the potential to be the first diagnostic imaging technology in coherent optics ^[2.7, 2.8]. OCT uses a broadband light source to perform high resolution cross-sectional tomographic imaging. However, even though a broadband light source supports a massive amount of imaging information, the method bears a problem called chromatic dispersion. As spectral band width of a light source increases, the dispersion problem in imaging becomes more severe. Dispersion is a physical phenomenon where phase velocity of wave depends on its wavelength. In fact, the refractive index of any media is not constant but a function of wavelength ^[2.1]. As a result, location and shape of the coherence function in an imaging system are modified, and acquired imaging information is degraded. Better images may be obtained if the effect of dispersion is corrected or compensated.

To overcome the problem caused by dispersion, this research introduces a system to control dispersion. One method to characterize dispersion is to measure phase shift of each wavelength of light that passes through a dispersive media. In this chapter, we report work to verify a method introduced by comparing results of a mathematical simulation with that of an optical experiment using a standard dispersive medium, water.

2.3. METHODS

This study describes a mathematical simulation to verify the method of characterizing dispersion, and then confirms the method by comparing simulation results with experimental results from measurements of group delay. The mathematical simulation computes group delay by using refractive index of water over the wavelength range of a broadband laser source. An experiment measuring group delay of water is performed.

2.3.1. Simulations

2.3.1.1. Computing group delay

To determine the group delay caused by a dispersive sample, a coherence function is generated. The method to generate the coherence function is explained in Section 2.3.1.2. Imaginary part of the coherence function is computed using the Hilbert transform to build an analytic signal.

$$u^i(t) = \frac{1}{\pi} \int_{-\infty}^{\infty} \frac{u^r(\zeta)}{\zeta - t} d\zeta \quad (2.1)$$

where, $u^i(t)$ is imaginary part of the analytic signal, $u^r(\zeta)$ is the real part of the analytic signal which is acquired experimentally. Using a Fourier transformation, phase information of the analytic signal is obtained in the frequency domain. These procedures of mathematical calculation are depicted in Figure 2.1. Phase of the coherence function is linear in frequency with a non-dispersive sample. On the other hand, phase is a non-linear function in a dispersive sample. Computing the difference between phase functions of non-dispersive and dispersive samples is equivalent to determining the group delay caused by dispersion.

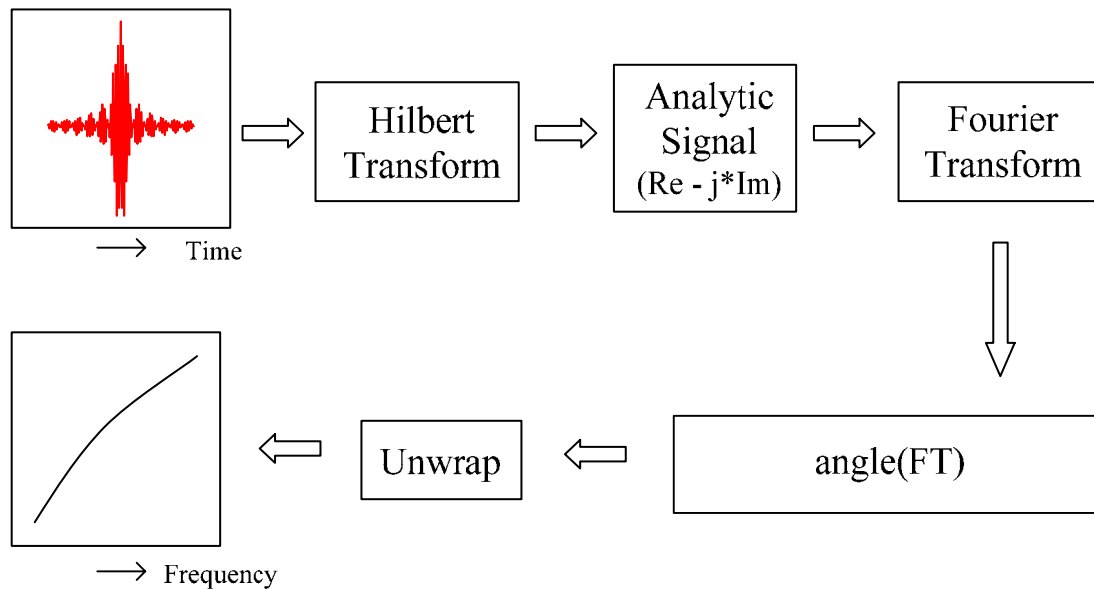


Figure 2.1. Procedure to compute group delay

2.3.1.2. Numerical Calculation of Coherence Function affected by Dispersion

To calculate the group delay of water as a dispersive sample, refractive index of deionized ultra filtered water (DIUF) over the wavelength range 800 - 900 nm of a broadband light source are utilized. The refractive index of DIUF water is shown in Figure 2.2 as measured by Bertie ^[2.9, 2.10]. The broadband light source is a Ti/Sapphire laser which has an 850 nm center wavelength (λ_0) and 80 nm spectral width ($\Delta\lambda$). The photon number spectral density of the light source is assumed Gaussian, which can be written as

$$N_s(\nu) = \frac{N_0}{\sqrt{2\pi} \cdot \Delta\nu} \cdot \exp\left(-\frac{(\nu - \nu_0)^2}{2 \cdot \Delta\nu^2}\right) \quad (2.2)$$

where N_0 is a constant for photon number,

ν_0 is the center frequency, and

$\Delta\nu$ is the spectral width of the light source.

The coherence function measured by an interferometer is

$$\Gamma(\tau) = \int N_s(\nu) \cdot \exp(i\Phi(\nu)) \cdot d\nu \quad (2.3)$$

where $\exp(i\Phi(\nu))$ is the complex conjugate of the dispersion phase coefficient of the sample and $\Phi(\nu)$ is the phase function,

$$\Phi(\nu) = \frac{4\pi\nu d}{c} \cdot [n_{H_2O}(\nu)] \quad (2.4)$$

where d is the sample thickness,

c is speed of light in vacuum, and

$n_{H_2O}(\nu)$ is refractive index of water.

Using Hilbert transformation of the coherence function, an analytic signal can be calculated. After Fourier transformation of the analytic signal, the phase information can be determined.

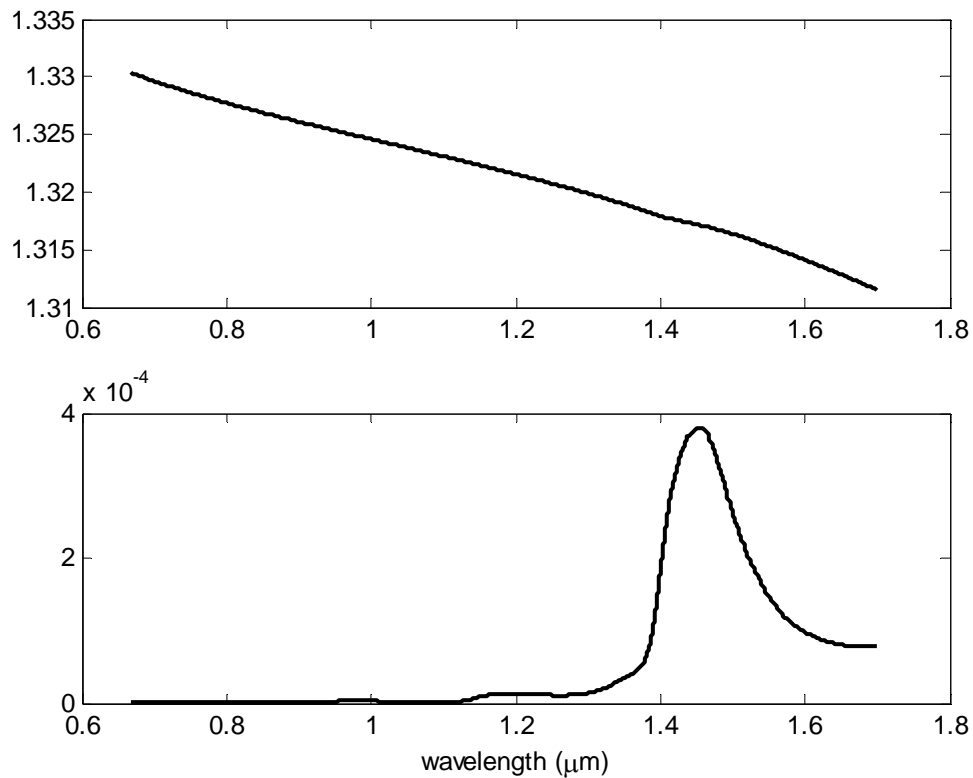


Figure 2.2. Refractive index of water; real part (upper) and imaginary part (lower) [2.9, 2.10]

2.3.2. Experiment

2.3.2.1. Dispersion Controller

The dispersion controller consists of a spatial light modulator (Cambridge Research and Instrument Inc., SLM-128), two lenses (JML Optical Industries Inc., achromatic triplet lens, $f/50.8$) and two gratings (Thermo RGL, $G=830.3/\text{mm}$). The layout is configured in a 4-f geometry as shown in Figure 2.3. Input light disperses from the surface of the first diffraction grating, is focused and dispersed in a horizontal plane. After passing through the first lens, the light is focused on the Fourier plane where the SLM is positioned. Shape of focused light is a horizontal line with each lateral position

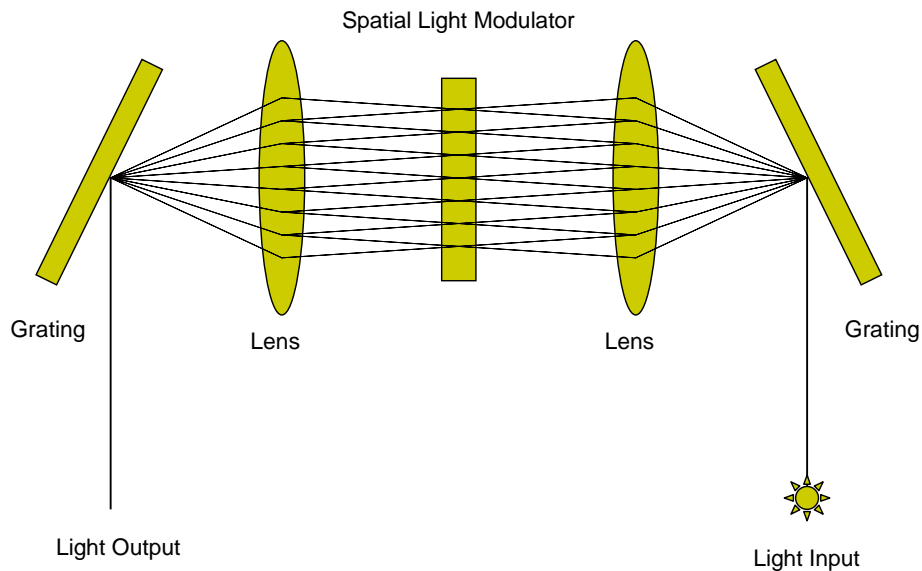


Figure 2.3. Diagram of dispersion controller

corresponding to a different wavelength. Light passes through the second lens and collimated by the second diffraction grating. Finally light returns and is shaped as the same beam profile as input light.

The liquid crystal window of the SLM has a 12.8 mm width and 2 mm height and 15 μm thickness. Along the width of the SLM, there are 128 individual pixels which are functionally identical. Each pixel of the liquid crystal has a 100 μm width and 2 mm height. The control unit of the SLM applies a voltage (12-bit) to each pixel to control the refractive index along horizontal axis. The fundamental idea to implement the SLM in an interferometer is that the group delay caused by a dispersive media in a sample path can be regulated by controlling optical path lengths in the SLM placed in the reference path of an interferometer (Figure 2.4).

2.3.2.2. Experimental Setup

The optical setup consists of a broadband light source, two beam splitters, a sample stage and a photodetector. The light source is a Ti/Sapphire laser; output wavelength range is from 800 nm to 900 nm. The light source is delivered through an optic fiber, collimated and input into the interferometer. The geometry of the interferometer shown in Figure 2.4 is different from that of a conventional Michelson interferometer. The setup uses two beam splitters which are not at 45 degrees with respect to incident light direction. The light source is split by the first beam splitter. One part of the light goes to the sample path and is reflected by the sample and goes to the photodetector (200-kHz Si Photoreceiver, New Focus). The remaining portion of light goes to the reference path; first, light passes through a dispersion controller and the

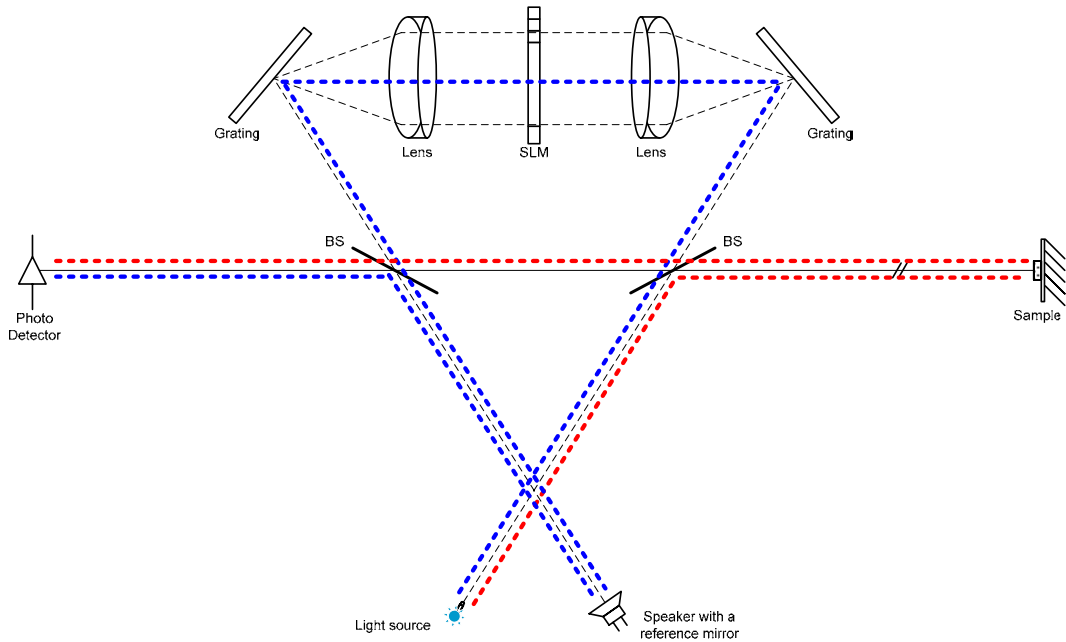


Figure 2.4. Optical experimental setup; interferometer with dispersion controller. Red dotted line: sample path, blue dotted line: reference path.

second beam splitter and is reflected by the reference mirror and the second beam splitter, and into the photodetector. The reference mirror is a retro-reflector and mounted on a loud speaker diaphragm that may be moved back and forward along a direction.

The detected signal from the photodetector is amplified and analog-to-digital converted by an amplifier (differential amplifier, LeCoy) and NI-DAQ (Data Acquisition Board, 12-bit, 500 kS/s, National Instrument), respectively. The wave generator creates a sine function for the speaker and trigger signal for the data acquisition board. The GPIB (general purpose interface board, GPIB+, National Instrument) send commands to the SLM controller to set phase delay in the liquid crystal window. Both the data acquisition

board and the GPIB are embedded in a personal computer and controlled by software coded in LabView. A block diagram of overall system is depicted in Figure 2.5.

2.3.2.3. Measurement of Group Delay caused by Water

To examine functionality of the system, we sought to measure group delay caused by water. The utilized sample in this experiment is deionized ultra filtered water (DIUF) contained in a 1 mm thick water chamber. The water chamber is made of glass that has a 140 μm thick microscope cover glass.

The water chamber has four surfaces for depth scanning; the front and back surfaces of each microscope cover glass. To measure group delay, the coherence function of the back surface of the glass located on back side is measured before and after filling the chamber with water. Reason for using the coherence function from the back surface is that the amount of reflected light from the front surface of the back glass would be

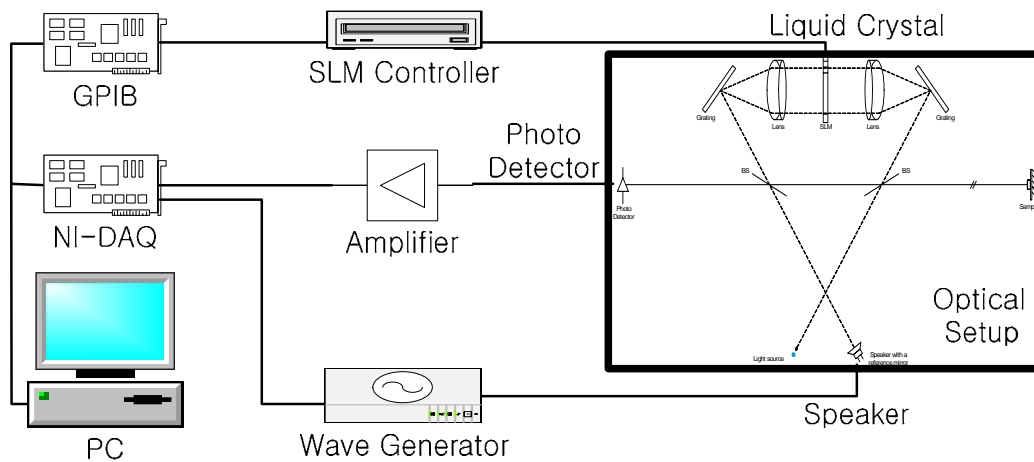


Figure 2.5. Block diagram of dispersion control system

changed after filling the water chamber with water because the relative refractive index is changed.

2.4. RESULTS

Results of calculating group delay using the Fourier transformed analytic signal of the coherence functions are presented in Figure 2.6 and Figure 2.7 as phase functions versus wavelength of incident light.

Figure 2.6-(a) shows two phase functions; the solid line is from the coherence

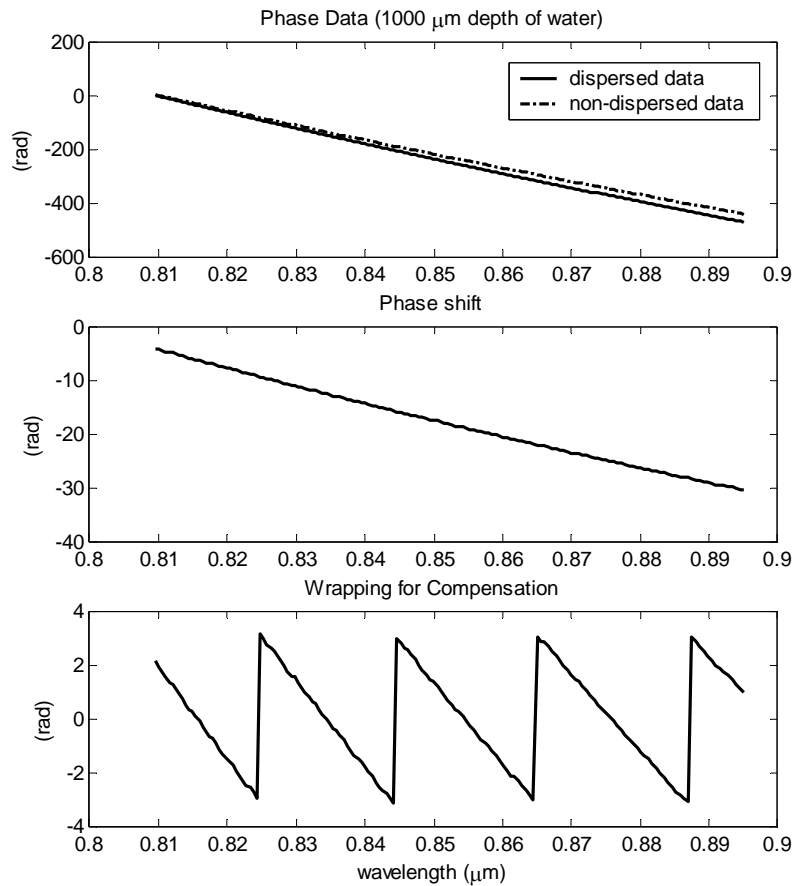


Figure 2.6. (a) top: phase data of dispersed and non-dispersed coherence function in frequency domain, (b) middle: phase shift is difference between the two data in (a), and (c) bottom: wrapped phase shift data for SLM

function of the water sample with a 1000 μm depth. The dotted line is phase of the coherence function with no sample and represents non-dispersed data. The phase shift of each wavelength is drawn in Figure 2.6-(b). The two lines in Figure 2.6-(a) have a small difference in slope. However, 26 radians of variation are observed throughout entire wavelength range. The phase variation is wrapped into the $+\pi$ to $-\pi$ range to estimate an input function to the SLM. The wrapped phase function is shown in Figure 2.6-(c).

Amount of dispersion depends on sample depth and is shown in Figure 2.6-(b). Dispersion at each depth is determined by subtracting the phase value of 835 nm from that of 870 nm and plotting the variation (Figure 2.7). Two wavelengths are selected to compare simulation with experimental results. Range of depths is from 0 to 1500 μm with a 50 μm step. Relationship between dispersion and depth is more or less linear

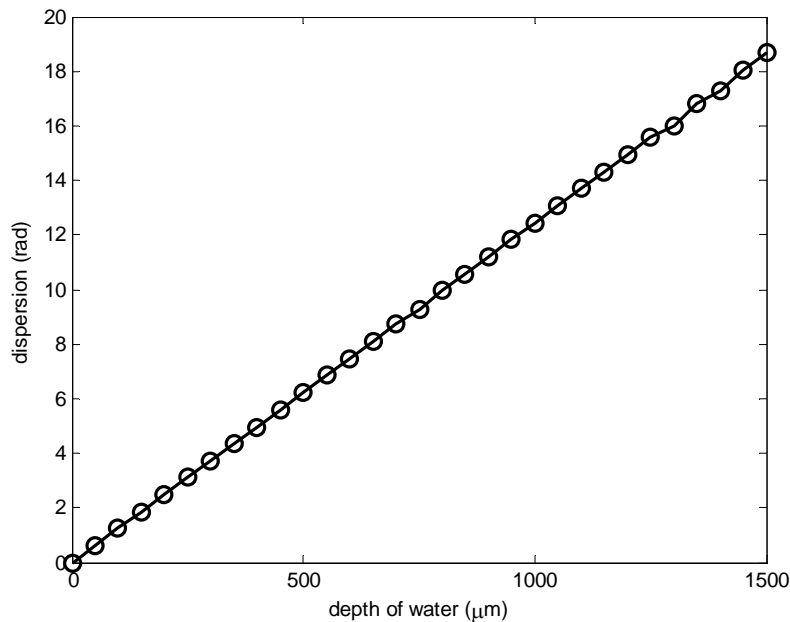


Figure 2.7. A graph of phase shift variation versus sample depth from simulation result

except for a couple of erroneous data points around 1350 μm .

The graph in Figure 2.8 depicts the experimental result of measuring the phase shift caused by water dispersion. The graph in solid line is the averaged over 20 measurements. Error-bars in the graph represent the standard deviation at each corresponding wavelength. The wavelength range (832 - 874 nm) of the measured data is limited to the Ti/Sapphire laser. Difference of phase, from 835 nm to 870 nm, is 25.42 radian in double pass, and the simulation result shows 24.90 radian in double pass; a difference of 0.52 radian over 42 nm.

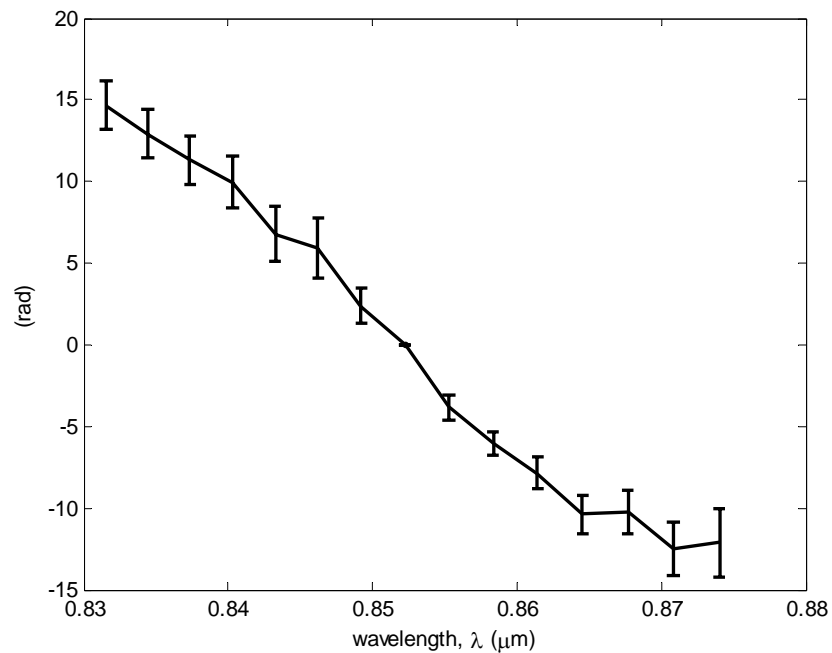


Figure 2.8. Phase shift versus wavelength (experimental data)

2.5. DISCUSSION

The phase function of dispersed data in the frequency domain shows a small amount of deviation from a linear function which is non-dispersed data. Difference between dispersed and non-dispersed data is the amount of group delay caused by the dispersive sample. Therefore, compensating the difference can be a way to eliminate the effect of dispersion. To implement the phase offset due to the liquid crystal of the SLM, the phase difference is wrapped. Wrapping occurs when the amount of phase variation from the calculation is larger than the maximum range of phase retardation in the SLM. According to a calibration graph provided by the manufacturer, the available linear control range of phase retardation in the SLM is 12 radian. Although the result of the amount of phase variation is smaller than the available control range, it is wrapped as shown as Figure 2.6-(c). Consequently the wrapped phase difference may be applied to compensate water dispersion.

According to Figure 2.7, amount of dispersion is proportional to thickness of the dispersive sample. Slope in the graph is about 24.89 (rad/mm, double path). Thus, optical path length in the sample can be estimated from measuring the amount of dispersion. The erroneous data from 1300 to 1450 μm in Figure 2.7 may be due to poor selection of wavelength range for phase analysis.

The experimental results show relatively stable data and are similar to the results of mathematical simulation. According to the simulation result in Figure 2.7, the amount of dispersion at 1000 μm is 24.89 radian, experimental result shows 25.42 radian, and the error is 2 %. The measured phase shift function from the system may be subjected to a dispersion compensating function produced by the SLM.

2.6. CONCLUSION

This study simulates group delay of a coherence function in the frequency-domain caused by dispersion in optical imaging. Water is used as a dispersive sample. An experiment to measure group delay caused by 1 mm thick water sample is performed to test feasibility of this approach. In conclusion, dispersion in optical imaging can be evaluated by phase analysis of the coherence function in frequency domain. Also, linearity between amount of dispersion and path length of sample is evident. In the case of water, the proportional constant of variation of phase shift versus depth is 24.89 (rad/mm) in a double pass. In addition, the experimental setup of this study may be used to measure group delay caused by a dispersive material and the system may be used to generate a function to vary group delay introduced by a material.

2.7. REFERENCES

- [2.1] Born M and Wolf E, *Principal of optics 7th ed.*, p.14-24, Cambridge University Press, Cambridge, 1999.
- [2.2] Walmsley I, Waxer L, Dorrer C, The role of dispersion in ultrafast optics, *Review of Scientific Instruments*, **72**(1), 1-29, 2001.
- [2.3] Milner TE, Class Notes of Noninvasive Optical Tomography in Spring 2003, BME389J in the University of Texas at Austin., 2003.
- [2.4] Brakenhoff GJ, van der Voort HTM, van Spronsen EA, Linnemans WAM, and Nanninga N, Three-dimensional chromatin distribution in neuroblastoma nuclei shown by confocal scanning laser microscopy, *Nature*, **317**, 748-749, 1985.
- [2.5] Boyde A, Stereoscopic images in confocal (tandem scanning) microscopy, *Science*, **230**(4731), 1270-1272, 1985.
- [2.6] Morgan F, Barbarese E, and Carson JH, Visualizing cells in three dimensions using confocal microscopy, image reconstruction and isosurface rendering: application to glial cells in mouse central nervous system, *Scanning Microscopy*, **6**(2), 345-356, 1992.
- [2.7] Brezinski ME and Fujimoto JG, Optical Coherence Tomography: High-Resolution Imaging in Nontransparent Tissue, *IEEE Journal of selected topics in quantum electronics*, **5**(4), pp.1185-1192, 1999.
- [2.8] Bordenave E, Abraham E, Jonusauskas G, Tsurumachi N, Oberle´ J, Rullie` re C, Minot PE, Lasse` gues M, and Bazeille JES, Wide-field optical coherence tomography: imaging of biological tissues, *Applied Optics*, **41**(10), 2059-2064, 2002.
- [2.9] Bertie JE and Lan Z, Infrared Intensities of Liquids XX: The intensity of the OH stretching band of liquid water revisited, and the best current values of the optical constants of H₂O(l) at 25°C between 15,000 and 1 cm⁻¹, *Applied Spectroscopy*, **50**(8), 1047-1057, 1996.
- [2.10] Bertie JE and Lan Z, The refractive index of colorless liquids in the visible and infrared: contributions from the absorption of infrared and ultraviolet radiation and the electronic molar polarizability below 20500 cm⁻¹, *Journal of Chemical Physics*, **103**(23), 10152-10161, 1995.

Chapter 3: Method to Calibrate Spatial Light Modulator (SLM) using Differential Phase Optical Coherence Tomography (DPOCT)

3.1. INTRODUCTION

Spatial light modulators (SLM) can modify properties of light, including amplitude, phase, and polarization. Because of their versatility SLMs have been utilized in optical research areas ^[3.1-3.6]. Enhanced optical imaging with adaptive optics research employs an SLM to correct wave-front errors ^[3.1]. Also SLMs are used as a space-switch or an optical cross connector, in telecommunication research due to their characteristic high power transmittance ^[3.2]. Moreover, fine control of phase retardation with SLM allows one to manipulate pulse shaping of ultra fast lasers ^[3.3-3.6].

For any application, measuring the phase response of an SLM is a prerequisite. The optical phase delay introduced by the SLM to an electrical input, must be calibrated before use. Generally the SLM manufacturer provides product data sheets including calibration data, but SLM users need to calibrate since each SLM product has variations, and manufacturers utilize different light sources. Two methods for calibrating SLM have been reported. The traditional technology from over two decades ago is based on interference signal analysis using a Mach-Zender interferometer ^[3.7]. Mach-Zender interferometers are vulnerable to environmental noises and require sensitive alignment of optical components. The other method for SLM calibration employs Young's fringes ^[3.8].

This method yields high precision and good stability, but requires long calculation after data collection due to its sophisticated mathematical theory.

We suggest a new method of SLM calibration using differential phase optical coherence tomography (DPOCT). DPOCT is capable of measuring optical path length difference (OPD) with high precision, high resolution, high speed, less noise from environmental perturbations, straightforward theory, and low-cost construction. DPOCT technique has been utilized to create a differential phase-contrast tomogram using a bulk interferometer ^[3.9]. Subsequently DPOCT has been implemented using a fiber based interferometer which incorporates two polarized light channels ^[3.10, 3.11]. As a consequence of its advantages, DPOCT has been employed in numerous optical path length difference measurements for several research applications. DPOCT has been applied to measure quantitative phase-contrast images ^[3.12, 3.13], to monitor photothermal and photoacoustic effects of laser-tissue interaction ^[3.14], to evaluate neural activity by measuring transient surface displacement of a neuron ^[3.15], and to determine concentration of biological aqueous solutions ^[3.16].

In this chapter, we present a method of SLM calibration using a fiber-based DPOCT. The optical experimental system and detailed experimental procedures are described.

3.2. METHODS

To calibrate a SLM, we measure the phase delay introduced by the SLM using DPOCT. This method section consists of Experimental system, SLM, DPOCT, and Experimental procedure.

3.2.1. Experimental System

Figure 3.1 illustrates an overall view of a fiber-based dual-channel phase-sensitive DPOCT system. Sample path optics of this system are depicted in Figure 3.2. Each component of the system is described following the order of light propagation. As shown in Figure 3.1, the system is a fiber based Michelson interferometer. DPOCT system consists of optic fibers, a path of light input, a sample arm, reference arm, and detection path. The optic fibers used in the system are polarization maintaining (PM) Fujikura Panda fiber. PM fiber has two orthogonal birefringent axes which have different refractive indices due to an internal stress structure. In the path of light input, the main light source of the system is a solid state diode laser (BBS 1310B-TS, ACF Technologies) which has 1.31 μm of center wavelength and 60 nm FWHM of bandwidth. An aiming beam (633 nm) is utilized for system alignment. Light from the broadband source and aiming beams are combined using a 2x1 optical coupler, and then input into Lyot depolarizer^[3,17]. Lyot depolarizer modifies the partially polarized beam of the light source to two equal amplitude linearly polarized beams. By splicing the PM fiber at 45°

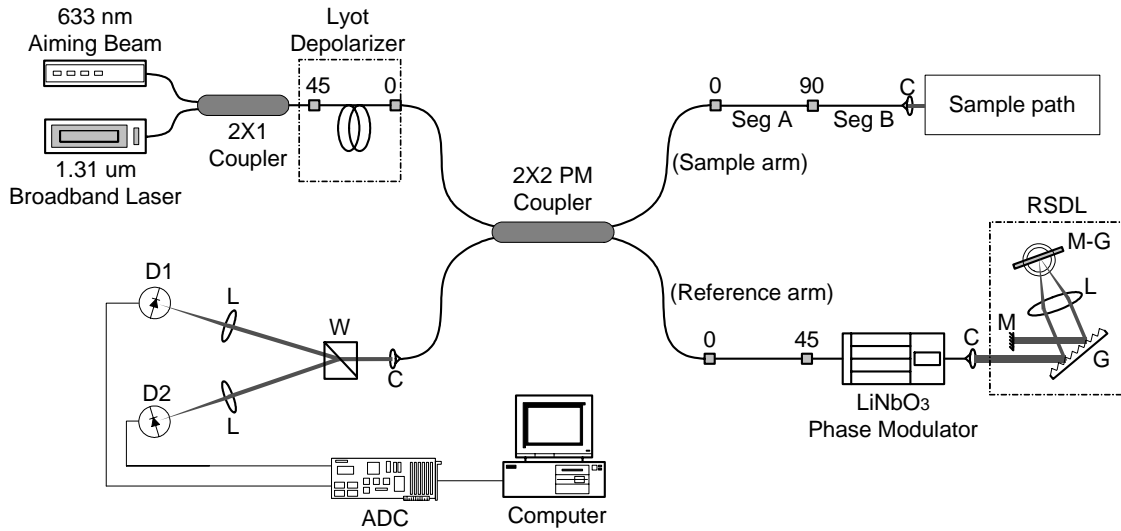


Figure 3.1. Experimental system; L: lens, M: mirror, M-G: mirror mounted on Galvanometer, G: grating, C: collimator with FC/APC optical connector, W: Wollaston Prism, D: photodetector, Seg: segment, ADC: analog to digital converter, RSDL: rapid scanning delay line, small squares and numbers above represent spliced locations and angles.

with respect to each other, the polarized beams are totally decorrelated by passing through birefringent PM fiber. In other words, the two orthogonally polarized beams are temporally delayed. The beams are input into a 2x2 PM coupler (Canadian Instrumentation) and split 50:50 into sample and reference arms.

In the sample arm, one PM fiber is spliced at 0° and another is spliced at 90° . The PM fiber is divided into two pieces and spliced at 90° to make equal optical path lengths of the two orthogonal axes. The rectangular feature terminating the end of the sample arm is described later (Figure 3.2).

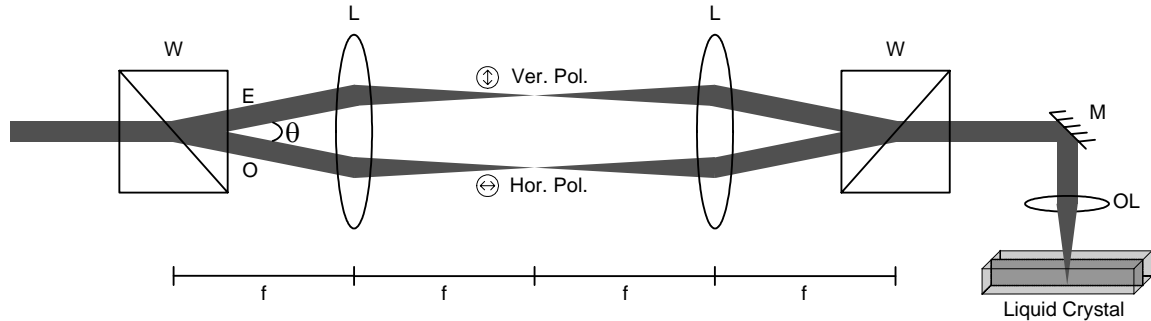


Figure 3.2. A detailed view of sample path with light trace; L: Triplet lens, W: Wollaston prism, OL: microscope objective lens, E: extraordinary axis, O: ordinary axis, f: focal length of the triplet lens, θ : diverged angle (2°), 4-f geometry with two lenses and two Wollaston prisms.

The reference arm includes a Lithium niobate (LiNbO_3) Y-waveguide phase modulator (JDS uniphase) and a rapid scanning delay line (RSDL) ^[3.18]. The PM fiber is spliced at 0° on the coupler side and 45° on the side connected the Lithium niobate phase modulator. Linearly polarized beams are equally divided into two axes again by a 45° splice and modulated by a multiple of π phase delay with the Lithium niobate phase modulator ^[3.11]. RSDL located at the end of the reference arm minimizes the material dispersion introduced by the Lithium niobate phase modulator by compensating the optical path length at different wavelengths. The RSDL modulates path length in the reference arm by tilting the mirror mounted on a galvanometer.

In the detection path, back reflected light from reference and sample arms recombine in the 2x2 PM coupler and is coupled to a collimator (PAF-X-11-IR, OFR)

through a FC/APC optical connector. A Wollaston prism splits light from the collimator into two polarization channels that diverges at 20° . The two photodetectors (Photodetector 2011, New Focus) measure intensity of each polarized light channel focused by the lenses. The measured data is digitized by a 12-bit analog to digital converter (CompuScope 12100, GaGe applied technologies) and stored in a workstation computer.

Figure 3.2 shows a magnified view of the sample path in the DPOCT system. The sample path consists of two Wollaston prisms, two triplet lenses, a mirror, a 10x microscope objective lens, and the uncovered liquid crystal part of the SLM. Input light is split to horizontally and vertically polarized light and diverged at 2° by the first Wollaston prism. The diverged light propagates parallel to each other and focused at focal plane after passing through the first lens. The second lens converges and the second Wollaston prism combines the light. Finally, the combined light is reflected by the mirror and focused on the front and back surface of the liquid crystal by the objective lens. The light reflected from the liquid crystal goes back to the 2x2 coupler retracing its path.

Because of the birefringence of the Wollaston prisms, the light of extraordinary axis travels a longer optical path length than that of the ordinary axis. This phenomenon is crucial for DPOCT system to locate the two individual interference fringe signals at the same position: one fringe signal from front surface and the other from back surface of SLM liquid crystal. The optical path length difference due to light propagation in SLM can be compensated by adjusting lateral position of the Wollaston prisms. As a consequence, the vertically polarized light in the sample path which passes through extraordinary axis is directly reflected from the front surface of the liquid crystal and then detected by photodetector 1, while the horizontally polarized light passing through ordinary axis travels through the SLM and is reflected from the back surface and detected

by photodetector 2. The two polarized light beams are decorrelated by the Lyot depolarizer as mentioned earlier.

3.2.2. Spatial Light Modulator (SLM)

Two major types of SLMs exist a micromechanical SLM and a liquid crystal SLM. Moreover, in terms of input, SLMs are categorized into optically and electrically addressed input SLM. The SLM used in this paper is a liquid crystal type and electrically addressed input SLM (SLM-128, Cambridge Research and Instrumentation). The SLM consists of a controller and a liquid crystal window as shown in Figure 3.3 and interfaces to a computer through an IEEE-488 PCI board. The SLM adjusts optical properties of its liquid crystals by applying various electrical voltage input to each liquid crystal. An applied voltage modifies refractive index along one direction of the liquid crystal but does not change its physical thickness. In other words, SLM varies optical path length of one polarization propagating through the liquid crystal. Because of this function, SLM is broadly used as an optical phase modulator. The input voltage range of the SLM is 0 to

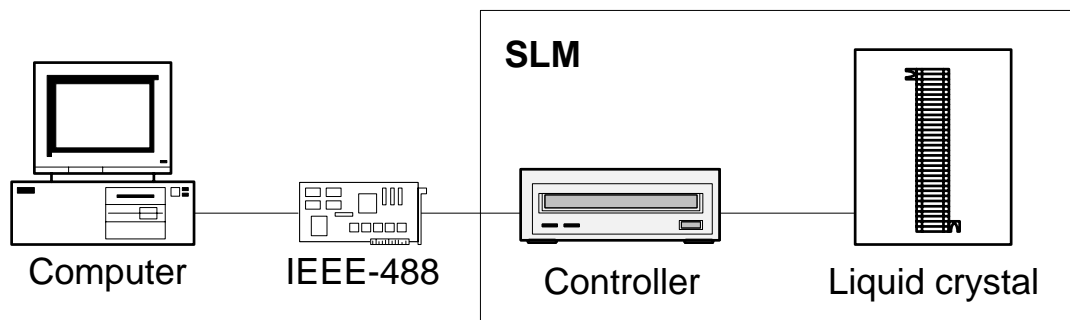


Figure 3.3. SLM consists of a controller and a liquid crystal window.

10 V with 0 to 4095 digital levels corresponding to an input resolution of $10/4096 = 2.441 \mu\text{V/bit}$. Input control is performed by the IEEE-488 board (GPIB+, National Instrument) with a control program coded in Labview. The liquid crystal has a 128-element-array with a 2 mm height and 12.8 mm total width. Each element of the 128-element-array is functionally independent to the others and has 2 mm height, $97 \mu\text{m}$ width, and $15 \mu\text{m}$ thickness. The liquid crystal modulates only horizontally polarized light.

3.2.3. Differential Phase Optical Coherence Tomography (DPOCT)

An excellent feature of DPOCT is dramatic reduction of phase noises due to stochastic environmental perturbations. The main theory of this feature is, first of all, to polarize light into horizontal and vertical axes and then to make longer optical path length on vertically polarized light and shorter optical path length on horizontally polarized light using Wollaston prisms to introduce an phase lag between the two polarized light beams. The amount of phase lag introduced is proportional to lateral position of the Wollaston prism. The sensitivity of phase lag can be estimated using the following equation.

$$\frac{\Delta\Phi}{\Delta x} = \frac{4\pi \Delta n \tan(\alpha)}{\lambda_0} \left(1 + \frac{1}{\cos\left(\frac{\theta}{2}\right)} \right) \quad (3.1)$$

where $\Delta\Phi$ is the double-path phase difference between the two orthogonal axes,

Δx is the lateral position of the Wollaston prism,

Δn is birefringence of quartz in the Wollaston prism: $\Delta n = n_e - n_o$ is

$$1.54282 - 1.53410 = 0.00872.$$

λ_0 is the center wavelength of the DPOCT source output, 1310 nm,

α is the cut angle in the Wollaston, 45° , and

θ is diverging light angle from the Wollaston, 2° .

As a result, the phase lag sensitivity, $\Delta\Phi/\Delta x$, of the system used in this paper is

$$96.59 \text{ (rad/mm) or } 0.966 \text{ rad/10 } \mu\text{m}.$$

The fundamental idea to measure the electro-optical phase response of SLM is to monitor the phase difference between two interference fringes in response to an input voltage; one from the front surface of the SLM liquid crystal and the other from the back surface. Varying the input voltage alters only the optical path length of light propagating through the liquid crystal. Observing the change of the phase difference with applied voltage gives calibration of the electro-optical phase response.

Vertically polarized light including the interference fringes of the front surface of the SLM liquid crystal is measured by photodetector 1, and horizontally polarized light propagating through the SLM is measured by photodetector 2. The measured intensity signal of the interference fringe formed in each photodetector is

$$I_m(z) = 2I_0 \sqrt{R_r R_s} \times \exp\left(-\frac{(z-z_0)^2}{l_c^2}\right) \times \cos(2\pi f_0 t + \varphi_m + \varphi_n) \quad (3.2)$$

where I_0 is a scale factor,

R_r and R_s are the reflectivity of reference and sample path, respectively,

l_c is the coherence length of the light source which is 22 μm ,

f_0 is the modulation frequency,

φ_m is the phase term which contains the differential phase information,

m is photodetector number (1 or 2), and

φ_n is common mode phase noise detected by both photodetectors. Finally the differential phase, $\Delta\varphi$, can be calculated by the following equation.

$$\Delta\varphi = \varphi_1 - \varphi_2 = 2\left(\frac{2\pi}{\lambda_0}\right)\Delta p = \frac{4\pi}{\lambda_0} \int_0^t n(z) dz \quad (3.3)$$

where $\Delta\varphi$ is the differential phase between φ_1 and φ_2 ,

Δp is optical path length difference,

t is the thickness of the sample, and

n is a function of refractive index in terms of depth, z .

More detailed explanation of the mathematical equations can be found in Reference [3.11].

3.2.4. Experimental Procedure

Experimental procedure is given in three parts: 1) alignment of optical components, 2) data collection with the experimental system, and 3) data processing of measured data. Before recording data the system must be aligned to locate interference fringe signals at the same position. First, the reference mirror mounted on the galvanometer in RSDL is activated in order to vary reference path length. The Lithium niobate phase modulator generates a 50 kHz carrier frequency for the fringe signals. Next, reflected light from the liquid crystal is maximized by adjusting axial location of the objective lens in the sample path. Optical path length of the reference arm is adjusted to equal that in the sample arm. Once interference fringes formed from the front surface of the SLM liquid crystal is found in both photodetectors, the other interference fringe can be found by adjusting lateral position of the Wollaston prism in the sample path. Finally, optimal alignment of the system is achieved by confirming that both interference fringes are positioned at same location in time. For data collection, the galvanometer in RSDL is deactivated and fixed. The Lithium niobate phase modulator is operated at 50 kHz and modulates 2π magnitude of the center frequency for continuous signal. The two photodetectors filter the measured signal at 3 kHz - 100 kHz and amplify at a gain of 10^3 . The output signals of both photodetectors are digitized by the analog to digital converter. Sampling rate is set at 10^7 samples/second and sampling duration at 1 second.

The lowest voltage, which designates level 0 in the control program, is applied to one element of the SLM for the first measurement. The total number of levels used for experimental measurements is 40 out of 4096 levels, for example, 0, 50, 100, 150, 200, 250, ..., 3250, 3500, 3750, 4095. After measurement at all levels for the first element is

finished, the SLM liquid crystal is moved laterally to allow measurement of the phase response of another liquid crystal element. The phase response measurement is repeated with another 9 randomly selected elements.

To extract phase difference between the two interference fringe signals, data processing of the collected data is performed in Matlab (Ver. 6.5). First, the raw fringe data of both signals is applied by Hilbert transforming to determine analytic signals consisting of real and imaginary values, and then, phase data can be derived from the analytic signal. Next, phase data is unwrapped to avoid phase jumps of 2π . Finally, phase difference between the two signals is calculated by subtracting phases. Following this approach, phase difference versus all 40 levels is estimated.

3.3. RESULTS

To calibrate phase response of a SLM liquid crystal, we measure interference fringe signals generated from the front and back surface of the liquid crystal using DPOCT, and phase difference between the two interference fringe signals is calculated.

The accuracy of differential phase from the DPOCT is about 0.05 rad which is 5.21 nm of optical path length in single pass. The coherence length of the light source is 28 μm in air. Positions of both Wollaston prisms are laterally displaced by 1.34 mm to compensate optical path length difference between horizontally and vertically polarized light.

Figure 3.4 depicts the phase response of the SLM. The y-axis of the graph is phase retardation in radians (left side) and nanometers (right side). The center wavelength of the light source is 1310 nm. The function of phase retardation in nm can be easily converted to another wavelength depending on a light source. The x-axis of the graph is the input level and is linearly proportional to electric voltage from 0 to 10 V. The data plotted as circles is mean of 10 measurements from each of 10 randomly selected SLM liquid crystal elements, and the solid line is the interpolated data. The function of phase retardation increases from zero to about 28 rad as voltage level increased. An ‘S’ shape of phase response is typical result of SLMs. The standard deviation of 10 measurements from same element at each of the 40 selected levels is shown in Figure 3.5. As Figure 3.4, the x-axis of the graph in Figure 3.5 is input level, and the unit of y-axis is radians. All 10 measurements are normalized by the value of the 800 level. The phase value at voltage of 800 is zero. All data in Figure 3.4 and Figure 3.5 are in double pass.

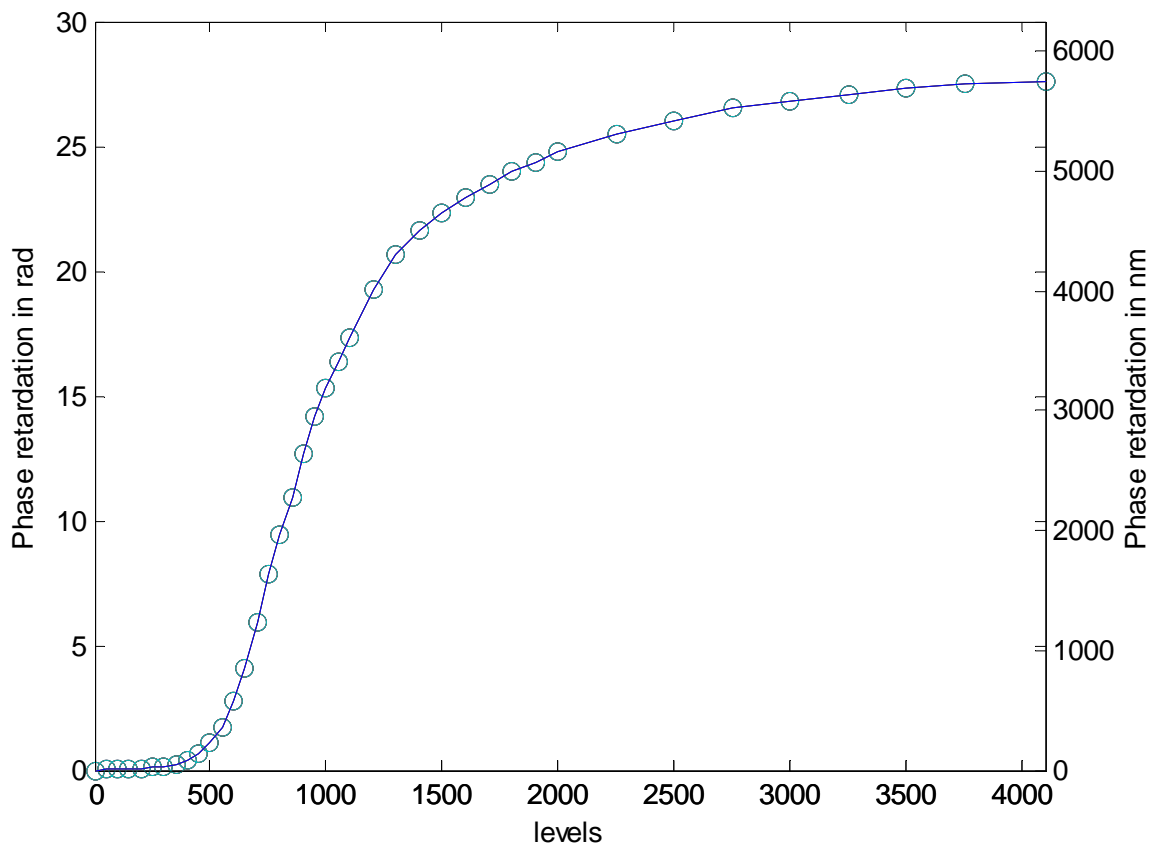


Figure 3.4. A graph of the electro-optical response of the SLM liquid crystal. Data is a double pass, mean of 10 liquid crystal cells. Range of levels (0 to 4095) with respect to electric input voltage (0 to 10 V).

3.4. DISCUSSION

Because differential phase is a relative measure, the phase response function in Figure 3.4 is frequently presented as an inverted ‘S’ shape. The range of practical usage of the SLM is from the 600 to 1000 levels which shows a linear response. Compared to limited information of input control range and lower resolution from manufacture’s data, this experimental result using DPOCT shows excellent resolution (5.21 nm) over the full control range. Also, performance of the DPOCT system shows a consistently measured phase difference at low variation. As shown in Figure 3.5, deviation of calibration data is up to 0.18 rad which is minimal compared to 28 rad of total range (~0.57% error). Benefits of DPOCT, such as high resolution and fast measurement, provide enormous feasibility to measure diminutive abrupt changes in optical path length in the SLM.

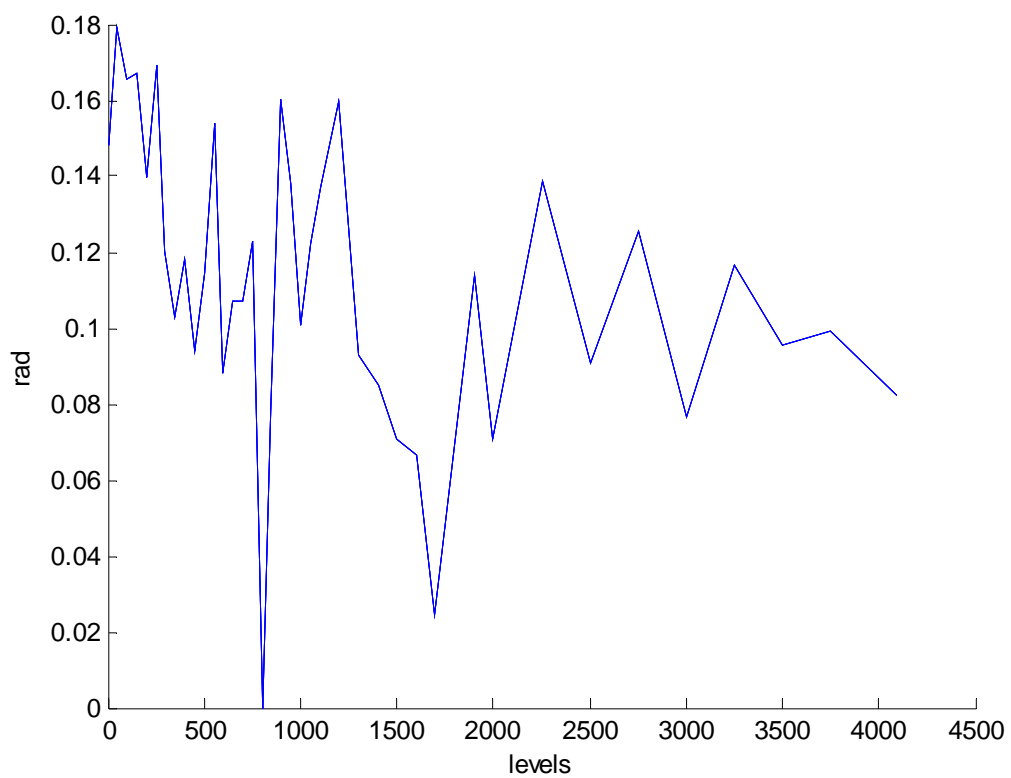


Figure 3.5. Standard deviation of 10 liquid crystal cells.

3.5. CONCLUSION

This chapter has provided a new method to calibrate phase response of a SLM using DPOCT. As mentioned in the Introduction and confirmed in Result, capability of sub-wavelength resolution (up to 5.21 nm) for measurement of transient change in optical path length allow use of DPOCT to calibrate the SLM. DPOCT has potential to significantly improve resolution and control range of current calibration methods such as the Mach-Zender and Young's interference fringes approaches.

3.6. REFERENCES

- [3.1] Shirai T, Liquid-crystal adaptive optics based on feedback interferometry for high-resolution retinal imaging, *Applied Optics*, **41**(19), 4013-4023, 2002.
- [3.2] Yu FTS and Jutamulia S, Spatial light modulators in telecommunication systems. *Proceedings of SPIE*, 4457,164-169, 2001.
- [3.3] Weiner AM, Heritage JP, and Kirschner EM, High-resolution femtosecond pulse shaping. *Journal of the Optical Society of America B*, **5**(8), 1563-1572, 1988.
- [3.4] Wang H, Zheng Z, Leaird DE, Weiner AM, Dorschner TA, Fijol JJ, Friedman LJ, Nguyen HQ, and Palmaccio LA. 20-fs Pulse shaping with a 512-element phase-only liquid crystal modulator, *IEEE Journal on Selected Topics in Quantum Electronics*, **7**(4), 718-727, 2001.
- [3.5] Suda A, Onish Y, Nagasaka K, Wang P, and Midorikawa K, A spatial light modulator based on fused-silica plates for adaptive feedback control of intense femtosecond laser pulses, *Optics Express*, **9**(1), 2-6, 2001.
- [3.6] Takada H, Kakehata M, and Torizuka K, Large-ratio stretch and recompression of sub-10-fs pulses utilizing dispersion managed devices and a spatial light modulator, *Applied Physics B*, **74**, S253-S257, 2002.
- [3.7] Martin-Badosa E, Carnicer A, Juvells I, and Vallmitjana S, Complex modulation characterization of liquid crystal devices by interferometric data correction, *Measurement Science and Technology*, **8**(7), 764-772, 1997.
- [3.8] Bergeron A, Gauvin J, Gagnon F, Gingras D, Arsenault HH, and Doucet M. Phase calibration and applications of a liquid-crystal spatial light modulator. *Applied Optics*, **34**(23), 5133-5139, 1995.
- [3.9] Hitzenberger CK and Fercher AF, Differential phase contrast in optical coherence tomography, *Optics Letters*, **24**(9), 622-624, 1999.
- [3.10] Dave DP and Milner TE, Optical low-coherence reflectometer for differential phase measurement. *Optics Letters*, **25**(4), 227-229, 2000.
- [3.11] Dave DP, Akkin T, Milner TE, and Rylander HG III. Phase-sensitive frequency-multiplexed optical low-coherence reflectometry, *Optics Communications*, **193**, 39-43, 2001.

- [3.12] Rylander CG, Dave DP, Akkin T, Milner TE, Diller KR, and Welch AJ, Quantitative phase-contrast imaging of cells with phase-sensitive optical coherence microscopy, *Optics Letters*, **29**(13),1509-1511, 2004.
- [3.13] Sticker M, Hitzenberger CK, Leitgeb R, and Fercher AF, Quantitative differential phase measurement and imaging in transparent and turbid media by optical coherence tomography. *Optics Letters*, **26**(8), 518-520, 2001.
- [3.14] Telenkov SA, Dave DP, and Milner TE, Low-coherence optical probe for non-contact detection of photothermal and photoacoustic phenomena on biomaterials. *Proceedings of AIP*, **657**(1), 852-858, 2003.
- [3.15] Akkin T, Dave DP, Thomas EM, and Rylander HG III, Detection of neural activity using phase-sensitive optical low-coherence reflectometry, *Optics Express*, **12**(1), 2377-2386, 2004.
- [3.16] Larin KV, Akkin T, Esenaliev RO, Motamedi M, and Milner TE, Phase-sensitive optical low-coherence reflectometry for the detection of analyte concentrations, *Applied Optics*, **43**(17), 3408-3414, 2004.
- [3.17] Mochizuki K. Degree of polarization in jointed fibers: the Lyot depolarizer, *Applied Optics*, **23**(19), 3284-3288, 1984.
- [3.18] Tearney GJ, Bouma BE, and Fujimoto JG, High-speed phase- and group- delay scanning with a grating-based phase control delay line, *Optics Letters*, **22**(23), 1811-1813, 1997.

Chapter 4: A Fiber-based Common-path Spectral Interferometer for Measurement of Higher-order Refractive Index and Dispersion

4.1. INTRODUCTION

Spectral interferometry (SI) has been widely used to measure optical properties of materials ^[4.1-4.23]. A fundamental feature of SI is the combination of an interferometer and spectrometer ^[4.3]. SI can provide spectroscopic information including spectral intensity, measurement of phase ^[4.4-4.6], optical path length ^[4.7-4.9], dispersion ^[4.10-4.17], and optical imaging ^[4.18-4.20] of a test material. Also, advanced SI methods have been recently developed and facilitated more convenient, stable, and accurate measurements. For example, a frequency swept laser source allows fast acquisition of high-resolution images ^[4.21, 4.22] and is used for a spectral polarimeter ^[4.23]. In addition, a common-path interferometer allows SI to be implemented as a compact, stable optical system with compensation of system dispersion ^[4.18, 4.19].

Dispersion, which results from higher-order refractive index variations in a material, can degrade the quality of optical images and result in artifacts in recorded images. To recognize and reduce effect of dispersion in optical imaging, several methods of dispersion research utilizing mathematical theories and employing additional optical components have been reported ^[4.10-4.17, 4.24]. Alternatively, dispersion can be a useful characteristic to identify a material and may be applied to determine material composition

of a sample similar to information obtained by absorption and transmission spectrophotometer measurements. Therefore measurement and analysis of material dispersion is a potentially valuable method in optical research and requires appropriate data processing.

This study reports a novel SI system and unique data processing procedure to estimate material dispersion. The SI system utilizes a high-resolution, broad-band frequency swept laser source and a fiber-based common-path interferometer, and integration of these components simplifies construction of the experimental system. To accommodate unevenly spaced optical frequency sampling in commercial swept laser sources, a non-uniform Fourier transformation ^[4.25-4.27] is used in data processing, and a multitaper spectral analysis method ^[4.28, 4.33] is applied. The data processing methods are robust and adaptive. Test material used in this study is deionized ultra high filtered water (DIUF) and glucose solutions. Furthermore, to verify the SI system and data processing methods, the experimental result is compared with that obtained from numerical calculation using refractive index of water measured by Bertie ^[4.34, 4.35].

In addition, optical technologies have been actively researched and progressed significantly in higher resolution and accuracy of glucose-monitoring ^[4.36-4.53]. Currently reported optical methods to measure glucose concentration are optical spectroscopy ^[4.37, 4.38], Raman spectroscopy ^[4.39-4.42], polarimetry ^[4.43-4.45], fluorimetry ^[4.47, 4.48], and interferometry ^[4.45, 4.47] analyzed with partial least squares ^[4.39, 4.41] and principal component analysis ^[4.50]. The most advanced optical method, optical coherence tomography (OCT), has been utilized to measure glucose concentration since 2001 ^[4.51-4.53] and provides more reliable results with higher accuracy. Despite outstanding performance of optical glucose-sensing methods, better sensitivity and accuracy of glucose measurement are demanded for practical usage in medical research.

This research proposes a novel optical method to quantitatively determine glucose concentration by use of swept-source spectral interferometry accompanied with Lomb-Scargle periodogram analysis ^[4.25-4.27] and multitaper spectral estimation ^[4.28-4.30] methods. The experimental data acquisition and analysis in this study are performed to estimate the resolution and accuracy of the proposed optical method to quantitatively determine concentration of an aqueous glucose solution in the range of 0-50 mM.

4.2. METHODOLOGY

This study reports a method to determine refractive index of a dispersive material using spectral interferometry (SI) and spectral phase analysis. Moreover, to quantitatively measure glucose concentration in an aqueous solution this study estimates the optical path length change of test solutions. Concentrations of test glucose solutions are in the range of 0-50 mM. The spectral interferometry system includes a frequency swept laser source and a common-path interferometer without requirement for mechanical scanning in the interferometer. Our spectral phase analysis incorporates two time-frequency transformation techniques; non-uniform Fourier transformation and multitaper spectral analysis. In this methodology, theory of the experimental SI system and data processing for spectral phase analysis are described.

4.2.1. Spectral Phase Analysis

Spectral phase analysis is used to analyze data measured from an interferometer in either the time-domain or spectral-domain. This section derives the mathematical equations to support spectral phase analysis of interference fringes recorded from a spectral interferometer.

Detected photon number spectral density at the output of a spectral interferometer is expressed as

$$N_D = |A_0|^2 \cdot \left[|s|^2 + |r|^2 + 2|s||r| \cdot \cos(2\pi\nu\tau + (\phi_s - \phi_r)) \right] \quad (4.1)$$

where $|A_0|^2$ is the number spectral density of the light source,

s is the amplitude of reflected light from the sample path,

r is the amplitude of reflected light from the reference path,

ν is optical frequency,

τ is optical time delay,

ϕ_s is the phase off-set of light reflected from the sample path, and

ϕ_r is the phase off-set of light reflected from the reference path.

Spectral phase variation is encoded in the cosine argument of Equation 4.1. The constant phase off-set between reference and sample paths, $(\phi_s - \phi_r)$, in the cosine argument can be small enough to be ignored in case of a stable optical system such as a common-path interferometer. The optical time delay, τ , is expressed as follows,

$$\tau = \frac{2\ell \cdot n}{C} \quad (4.2)$$

where ℓ is the physical path length difference between the reference and the sample,

n is the refractive index, and

C is the speed of light.

The factor of 2 is due to the double pass reflection through the sample. The interference term from Equation 4.1 with Equation 4.2 is

$$|A_0|^2 \cdot 2|s||r| \cdot \cos\left(\frac{4\pi \cdot \nu \cdot \ell \cdot n}{C}\right). \quad (4.3)$$

The spectral phase function is,

$$\varphi(\nu) = \frac{4\pi}{C} \cdot \nu \cdot \ell \cdot n(\nu). \quad (4.4)$$

The spectral phase function varies with refractive index and optical frequency. Here, refractive index of a dispersive material is assumed as a polynomial function in optical frequency,

$$n(\nu) = a_0 + a_1\nu + a_2\nu^2 + a_3\nu^3 + a_4\nu^4 + \dots. \quad (4.5)$$

In this study, however, the refractive index is written as a fourth order polynomial. In this case, spectral phase function is given by

$$\varphi(\nu) = \frac{4\pi}{C} \cdot \ell \cdot (a_0\nu + a_1\nu^2 + a_2\nu^3 + a_3\nu^4 + a_4\nu^5). \quad (4.6)$$

In case of a common-path interferometer, a spectral phase function formed by interference from a surface and reference can be expressed by

$$\varphi(\nu) = \frac{4\pi}{C} \cdot \ell \cdot (a_0\nu + a_1\nu^2 + a_2\nu^3 + a_3\nu^4 + a_4\nu^5) + (b_0 + b_1\nu). \quad (4.7)$$

where b_0 is added due to a phase unwrap constant, and b_1 is added due to the optical path length difference (OPD) between reference and sample in the system, and can be extended as $b_1 = \frac{4\pi}{C} \cdot OPD$.

If we let $c_0 = b_0 \cdot \frac{C}{4\pi \cdot \ell}$ and $c_1 = b_1 \cdot \frac{C}{4\pi \cdot \ell}$, and apply to Equation 4.7, the spectral phase function of the common-path interferometer is

$$\varphi(\nu) = \frac{4\pi}{C} \cdot \ell \cdot [c_0 + (c_1 + a_0)\nu + a_1\nu^2 + a_2\nu^3 + a_3\nu^4 + a_4\nu^5]. \quad (4.8)$$

Equation 4.7 and Equation 4.8 are used and discussed in the spectral interference analysis section (4.2.3.3.).

4.2.2. Experimental System

4.2.2.1. Measurement of Dispersion

The experimental system setup is depicted in Figure 4.1. The optical system is a fiber-based common-path spectral interferometer using a high-resolution, broad-band frequency swept laser source. This experimental system consists of three major parts; the light source, interferometer, and detector. The light source is a frequency swept laser (Precision Photonics, TLSA1000); wavelength range 1520-1620 nm, and maximum output power 0.4 mW. The spectral line width of the swept laser is specified at 150 KHz. The interferometer is a Michelson-type common-path interferometer and includes an

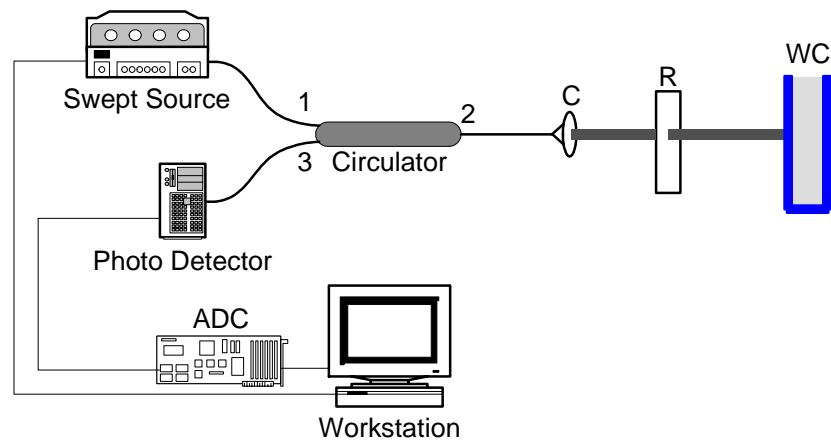


Figure 4.1. Fiber-based common-path spectral interferometer using a frequency swept laser source. 1, 2, and 3: port number, C: collimator, R: reference plate, WC: a water filled sample chamber.

optical circulator (GOULD fiber optics, CIRC-3-55-P-BB-106), a collimator (OFR, PAF-X-7-NIR), a reference plate, and a sample chamber. The reference plate is a borosilicate glass of 6.3 mm thickness, and the sample chamber holds the liquid sample and is constructed using microscope slides. The detector part is comprised of a photodetector (New Focus, photodetector 2011), an analog-to-digital converter (ADC) (National Instrument, AT-MIO-64E-3), and a computer workstation.

Input light generated by the swept laser source is coupled into port 1 and exits through port 2 of the optical circulator. Light exiting port 2 is collimated and passes through the reference plate and sample chamber. Incident light is reflected from the two surfaces of the reference plate and four surfaces of the water chamber. Reflected light interferes and returns to port 2 of the optical circulator. Interfering light exits the optical circulator through port 3 and is coupled into the photodetector. Optical intensity of interfering light is converted to an electric voltage signal, and is stored into the computer workstation after conversion by the ADC.

An important advantage of employing a frequency swept laser source is relaxation of the requirement for a mechanical scanning delay line in the reference path of the interferometer. Also the swept laser used in this study has a narrow spectral line-width that provides a flexible optical scanning range as long as three meters and a function that gives optical frequency of the emitted laser light. Instead of using two distinct sample and reference paths, the common-path interferometer provides a compact and stable optical system, reduces time and effort for optical alignment, and establishes automatic compensation of dispersion and phase off-set in the system up to the reference plate.

4.2.2.2. Measurement of Glucose Concentration

An overall view of the experimental system is illustrated in Figure 4.2. The optical system consists of three parts; a light source, an interferometer, and a detector. There is small modification from the system described in previous section; a plano-convex lens (Newport, plano-convex, BK7, $f = 50.2$) and another sample chamber (NSG Precision Cells Inc., ID = 2.686 mm).

The plano-convex lens functions as a reflector for the reference and a condenser that focuses the input light into the sample chamber and also focuses the reflected and scattered light from the surfaces of the sample chamber into the collimator. Therefore the

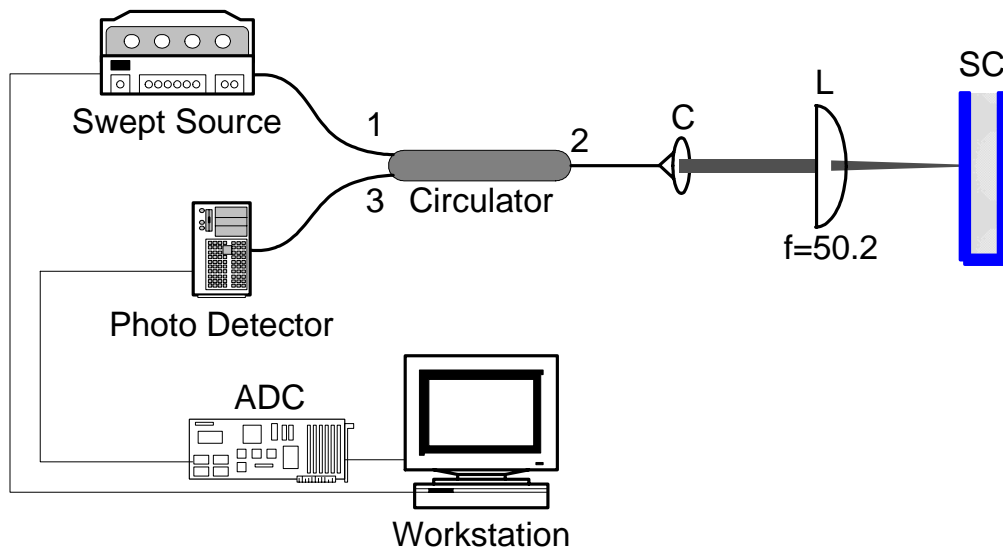


Figure 4.2. Experimental system: common-path spectral interferometer. C: collimator, L: plano-convex lens, SC: sample chamber, and ADC: analog-to-digital converter.

reference path for the common-path interferometer extends from the optical circulator to the front surface of the plano-convex lens.

Glucose solutions for experimental measurement are prepared at 6 concentrations for micro-ranges, 0 to 5 mM with 1 mM increments and 11 concentrations for macro-range, 0 to 50 mM with 5 mM increments. These solutions are diluted from a 50% liquid D-glucose (Abbott Lab, NDC 0074-6648-02).

20 measurements are recorded for each glucose solution, and measurements are achieved at room temperature (21°C). The temperature of the solution is not affected by any illumination or heat source during the experiment.

4.2.3. Data Processing

The spectral interference fringe data acquired from the experimental system depicted in Figure 4.1 is processed to extract higher-order refractive index of the sample for estimating the material dispersion. Raw data contains 15 interference fringe frequencies that are combinations of pairs of 6 reflections from each surface of the reference plate (2) and water chamber (4) in the common-path interferometer. To analyze the acquired data, raw data measured in the spectral domain is transformed to the optical time delay domain using a non-uniform Fourier transformation, which accommodates uneven data sampling of the swept laser. A multitaper spectral estimate is applied to the fringes comprised by light reflected from the sample. Finally, the spectral phase function is calculated from multitapered data. Each of the data processing procedures is described in detail in the following subsections.

4.2.3.1. Non-Uniform Fourier Transformation

The first task to analyze the raw data measured from SI is a time-frequency transformation to find fringe amplitude in the time delay domain. Because of the inconsistent frequency sampling interval from the swept laser source, interference fringe data is analyzed using a non-uniform Fourier transformation (NUFT) rather than the more common discrete Fourier transform (DFT) or fast Fourier transform (FFT) which require evenly spaced data. Most commercially available frequency swept laser sources generate

unevenly spaced frequency data. To accommodate non-uniform sampled data from the swept laser source a fast Lomb-Scargle algorithm is developed. The Lomb-Scargle periodogram is a novel method of Fourier spectrum analysis for unevenly spaced data [4.25, 4.26] and has been modified to a fast algorithm by Press and Rybicki [4.27].

Briefly, the normalized Lomb-Scargle spectral power density is computed by,

$$SPD(\omega_k) = \frac{1}{2\sigma^2} \left[\frac{\left\{ \sum_{i=1}^N (h_i - \bar{h}) \cos(\omega_k (t_i - \tau)) \right\}^2}{\sum_{i=1}^N \cos^2(\omega_k (t_i - \tau))} + \frac{\left\{ \sum_{i=1}^N (h_i - \bar{h}) \sin(\omega_k (t_i - \tau)) \right\}^2}{\sum_{i=1}^N \sin^2(\omega_k (t_i - \tau))} \right] \quad (4.9)$$

where \bar{h} and σ are the mean and variance of measured data $h_1, h_2, h_3, \dots, h_N$ acquired at times $t_1, t_2, t_3, \dots, t_N$, respectively. The time interval between successive times is not necessarily uniform. The parameter τ is defined as

$$\tan(2\omega_k \tau) = \frac{\sum_{i=1}^N \sin(2\omega_k t_i)}{\sum_{i=1}^N \cos(2\omega_k t_i)}, \quad (4.10)$$

and properties of τ are described in Reference [4.27]. Major sequences of the fast Lomb-Scargle algorithm incorporate Lagrange interpolation and FFT to reduce computation complexity.

4.2.3.2. Multitaper Spectral Analysis

Once spectral domain data is transformed to the time delay domain, the next procedure is spectral phase analysis after examining and windowing depth scan data. Traditional non-parametric spectral analysis integrating a single window or smoothing window (e.g., Gaussian, Blackman, and Hamming windows) is unavoidable to have substantial side-lobe energy leakage. The multitaper method for spectral analysis ^[4.28] employs a number of orthogonal tapers, called Slepian sequences or discrete prolate spheroidal sequences (DPSS) ^[4.29], rather than a single window, and consequently provides less side-lobe contamination while maintaining a stable spectral estimation. This method is adaptive and stochastic spectral analysis by applying weighted individual eigenvectors, which are tapered Fourier transformations of time series data. Numerous applications of multitaper spectral analysis have been reported in geophysical seismic applications ^[4.30-4.32] and in electrophysiological signal processing ^[4.33].

The general procedure for multitaper spectral analysis has three tasks. The first task is to find Slepian sequences based on number of sample data, N , and a given frequency-bandwidth parameter, W . Slepian sequences satisfy a Toeplitz eigenvalue equation ^[4.29],

$$\sum_{m=0}^{N-1} \frac{\sin\{2\pi W(n-m)\}}{\pi(n-m)} v_m^{(k)}(N, W) = \lambda^{(k)}(N, W) v_n^{(k)}(N, W). \quad (4.11)$$

for $k = 0, 1 \dots (2NW-1)$, where $v_n^{(k)}(N, W)$ is the k th Slepian sequence and $\lambda^{(k)}(N, W)$ is the k th eigenvalue.

In the second task, eigencefficients of the sample, $y(f)$, are calculated by Fourier transformation of the tapered time series sample data ^[4.28],

$$y_k(f) = \sum_{n=0}^{N-1} x(n) v_n^{(k)}(N, W) e^{-i2\pi f n} \quad (4.12)$$

where $y_k(f)$ is k th eigencefficient. For the last task of multitaper spectral analysis, the addition of eigencefficients with weights provides spectral estimates,

$$S(f) = \frac{\sum_{k=0}^{K-1} b_k |y_k(f)|^2}{\sum_{k=0}^{K-1} b_k} \quad (4.13)$$

where b_k is the weight of k th eigencefficient. The weights are adaptively established by an iterative process for each eigencefficient in order to optimize the tradeoff between variance and bias.

4.2.3.3. Spectral Interference Analysis

Depth scanning information resulting from application of the fast Lomb-Scargle algorithm using raw data measured by the fiber-based common-path spectral interferometer unveils the longitudinal structure of the test sample and the sample chamber. Interference fringe amplitude in time delay domain is shown in Figure 4.3. A simplified illustration of reference and water chamber used in this study is displayed in the box at the upper right corner of the figure. Numbers and letters in the box represent corresponding surfaces which reflect input light. The direction of input light is from left to right in the optical construction depicted in the figure. Labels of each interference fringe in the figure indicate the two surfaces where light is reflected and generate corresponding fringes.

For each scan of the swept laser, 15 interference fringes are generated by every combination of two reflected beams from the two surfaces of the reference plate and the four surfaces of the sample chamber. Interference fringes of interest for spectral phase analysis are generated by the back surface of the reference plate and both of the inner surfaces of the sample chamber and are labeled 2/B and 2/C as displayed in Figure 4.3. Even though one of the surfaces in the water chamber is able to act as a reference surface, the reference plate is employed to shift the location of the interference fringe away from DC noise which dominates near the origin. Locations of each fringe in Figure 4.3 provides the optical path length between the two surfaces reflecting the input light that generates the fringe. According to Equation 4.3, the ℓ indicates optical path length difference and is included in the cosine argument. Therefore the path length can be calculated by a proper time-frequency transformation.

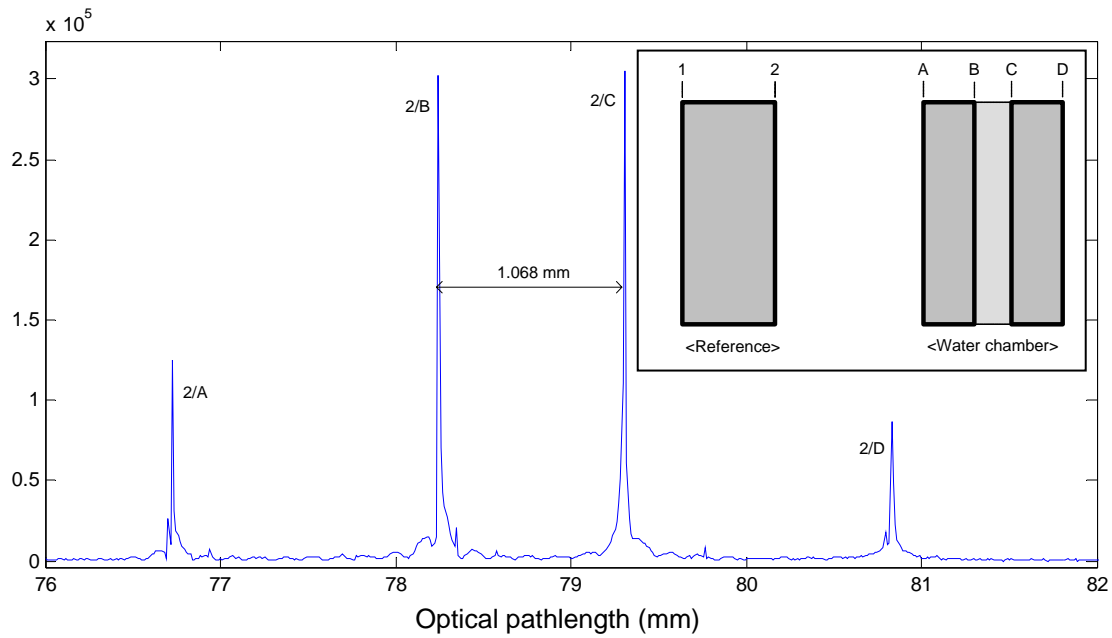


Figure 4.3. Interference fringes in path length difference domain. Sample path layout is given in inserted box. 1, 2, A, B, C, and D are labels for each surface. 2/A, 2/B, 2/C, and 2/D are labels for interference fringes corresponding to mixing of reflections from the two surfaces. Incident light propagates from left to right.

To calculate dispersion of water, the spectral phase function of the 2/B interference fringe containing dispersion of chamber glass wall is subtracted from that of 2/C interference fringe which includes dispersion of glass and water. In other words, light reflected from surface B travels only through the glass (not water) and interferes with light reflected from surface 2. Consequently the 2/B interference fringe has dispersion of the chamber glass. On the other hand, light reflected from surface C travels through both glass and water; hence the 2/C interference fringe includes dispersion of both glass and

water. Figure 4.4 illustrates a detail view of interfering beams. The two interference fringes, 2/C and 2/B are exclusively windowed and subjected to multitaper spectral analysis. Spectral interference fringes of 2/C and 2/B are calculated, and finally the spectral phase functions can be estimated by extracting the phase component of each pair. According to Equation 4.4 and Equation 4.7, the spectral phase functions of 2/C and 2/B can be expressed as,

$$\varphi_{\alpha}(\nu) = \frac{4\pi}{C} \cdot \nu \cdot \left[\ell_s \cdot n_s(\nu) + \ell_g \cdot n_g(\nu) + \ell_a \cdot n_a(\nu) \right] + b_{\alpha 0} + b_{\alpha 1} \nu \quad (4.14)$$

and

$$\varphi_{\beta}(\nu) = \frac{4\pi}{C} \cdot \nu \cdot \left[\ell_g \cdot n_g(\nu) + \ell_a \cdot n_a(\nu) \right] + b_{\beta 0} + b_{\beta 1} \nu, \quad (4.15)$$

respectively. The spectral phase function of water is

$$\begin{aligned} \varphi_s(\nu) &= \frac{\varphi_{\alpha}(\nu) - \varphi_{\beta}(\nu)}{2} \\ &= \frac{2\pi}{C} \cdot \nu \cdot \ell_s \cdot n_s(\nu) + \frac{(b_{\alpha 0} - b_{\beta 0}) + (b_{\alpha 1} - b_{\beta 1}) \cdot \nu}{2} \\ &= \frac{2\pi}{C} \cdot \ell_s \cdot (a_0 \nu + a_1 \nu^2 + a_2 \nu^3 + a_3 \nu^4 + a_4 \nu^5) + \frac{(b_{\alpha 0} - b_{\beta 0}) + (b_{\alpha 1} - b_{\beta 1}) \cdot \nu}{2} \end{aligned} \quad (4.16)$$

After subtracting the constant and the first order polynomial function which can be calculated by a linear least-square fitting from φ_s , the function is

$$\varphi_h(\nu) = \frac{2\pi}{C} \cdot \ell_s \cdot (a_1\nu^2 + a_2\nu^3 + a_3\nu^4 + a_4\nu^5). \quad (4.17)$$

Finally a spectral phase function exclusively containing higher-order refractive index of water is estimated.

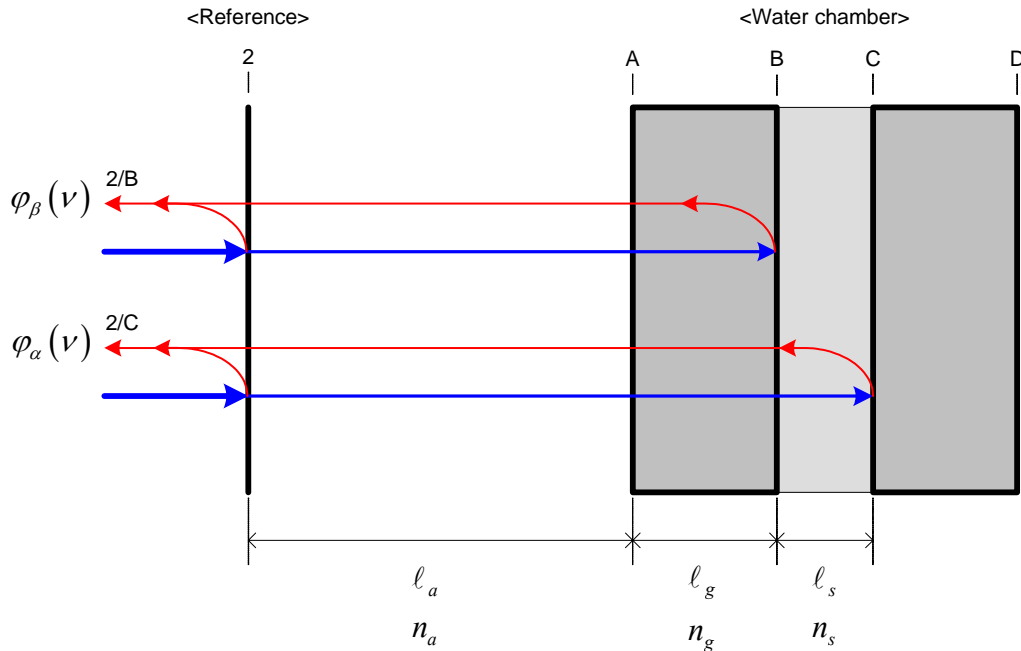


Figure 4.4. Detailed diagram of interferometer sample path. $\varphi_\alpha(\nu)$ and $\varphi_\beta(\nu)$ represent the spectral phase functions of 2/C and 2/B interference fringes, respectively. l_a , l_g , and l_s are physical path length in air, glass, and water; n_a , n_g , and n_s are refractive indices of air, glass, and water, respectively. The blue lines indicate light input while red are reflected light.

4.2.3.4. Optical Path Length Estimation

In glucose concentration measurement, interested interference fringes isolated in the time-delay domain computed by the NUFT of the raw data are selected and arranged in order to configure the location and the size of the window that are important parameters for multitaper spectral estimation. Figure 4.5 shows an illustration of the optical paths of the common-path interferometer to provide a convenient view to better

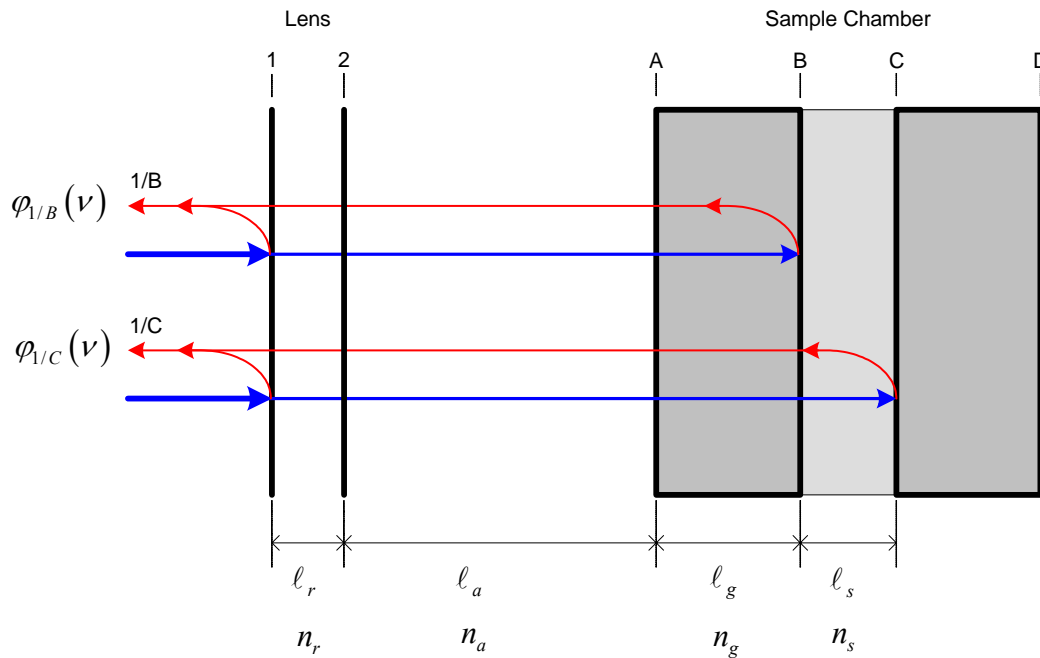


Figure 4.5. Detailed diagram of interferometer sample path. $\varphi_{1/C}(\nu)$ and $\varphi_{1/B}(\nu)$ represent the spectral phase functions generated from 1/C and 1/B interference fringes, respectively. ℓ_r , ℓ_a , ℓ_g , and ℓ_s are physical path lengths in lens, air, glass, and sample; n_r , n_a , n_g , and n_s are refractive indices of lens, air, glass, and sample, respectively. Thick blue lines indicate light input while red thin lines are reflected light.

understand how the common-path interferometer operates and is used to estimate location of interested interference fringes in the time delay domain. Single numbers and letters in Figure 4.5 represent corresponding surfaces which reflect incident light. The labels, 1/B and 1/C on the left side of Figure 4.5 indicate the interference fringes generated by the two surfaces where the light is reflected and are of interest for data processing. Figure 4.6 is a partial view of the NUFT result, with horizontal axis being optical path length in single pass. As Figure 4.6 indicates, location of fringes in the time delay domain can be estimated by optical path length difference (OPD) between reference and sample paths.

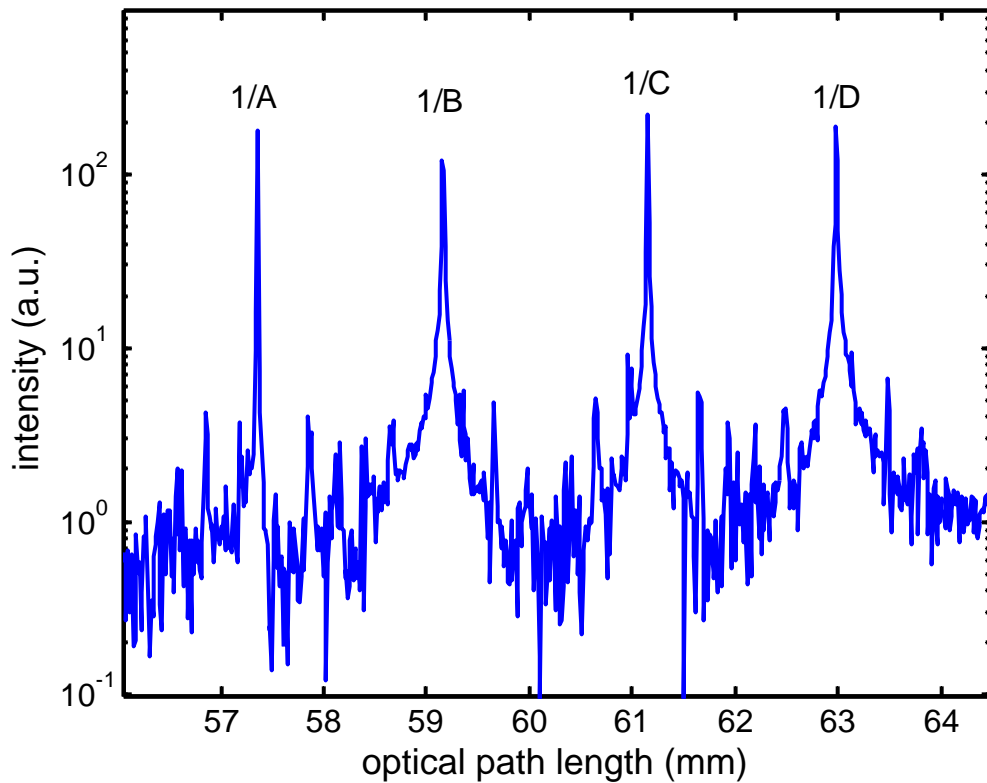


Figure 4.6. Interference fringe intensity versus optical path length computed from Lomb-Scargle periodogram analysis. This data provides the depth-scanned information of the optical construction of the sample chamber.

For the next, spectral phase functions of interested fringes, $\varphi_{1/C}(\nu)$ and $\varphi_{1/B}(\nu)$, are calculated from the results of multitaper spectral analysis of 1/C and 1/B, respectively, and can be modeled as,

$$\varphi_{1/C}(\nu) = \frac{2\pi}{C} \cdot \nu \cdot [\ell_r \cdot n_r(\nu) + \ell_a \cdot n_a(\nu) + \ell_g \cdot n_g(\nu) + \ell_s \cdot n_s(\nu)] \quad (4.18)$$

$$\varphi_{1/B}(\nu) = \frac{2\pi}{C} \cdot \nu \cdot [\ell_r \cdot n_r(\nu) + \ell_a \cdot n_a(\nu) + \ell_g \cdot n_g(\nu)] \quad (4.19)$$

where ℓ_r , ℓ_a , ℓ_g , and ℓ_s are physical lengths of the lens, air, glass, and sample; n_r , n_a , n_g , and n_s are refractive indices of lens, air, glass, and sample, respectively. By calculating the slope of $\varphi_{1/C}(\nu) - \varphi_{1/B}(\nu)$, optical path length of the sample can be extracted.

4.3. RESULTS

To determine higher-order refractive index of a test material and to estimate the optical path length of glucose solutions to quantitatively determine concentration of glucose, this study suggests a method that includes a novel spectral interferometer (SI) and unique data processing procedures.

Fortunately, the light source used in this study provides frequency data of the laser output. The frequency data is stored in the computer workstation directly through the universal serial bus (USB) connection from the light source. The mean frequency interval is 0.400 GHz and standard deviation (STD) is 0.0076 GHz.

In one of the experimental preparations, the sample chamber for holding the test material, water, is made of microscope slides, with 0.789 mm of inner space and 1 mm wall thickness. As a result of locating the reference plate at 80 mm in front of the sample chamber, interference fringes of interest are recorded away from the origin where DC noise dominates; Figure 4.3 shows fringe position in time delay domain (horizontal axis). The fast Lomb-Scargle algorithm provides a solution of the problem caused by unevenly spaced frequency samples in the swept light source and gives advantages of faster processing speed as well as less spectral leakage. The adaptively optimized weight factor of multitaper spectral analysis for this study is

$$b_k(N) = e^{-\frac{(N-N_0)^2}{2\sigma^2}} \quad (4.20)$$

where $N = 1, 2, 3, \dots, 8$, $N_0 = 6.5$, and $\sigma = 1.225$ for higher-order refractive index estimation; besides $N = 1, 2, 3, \dots, 8$, $N_0 = 0.75$, and $\sigma = 0.5$ for glucose measurement. Figure 4.7 shows the result of 20 experimental measurements from the spectral interferometer and spectral phase analysis. The thin solid line in Figure 4.7 is the mean of 20 spectral phase functions from Equation 4.17 of each measurement and exclusively contains the higher-order refractive index of water, and the thick dashed line is the 5th

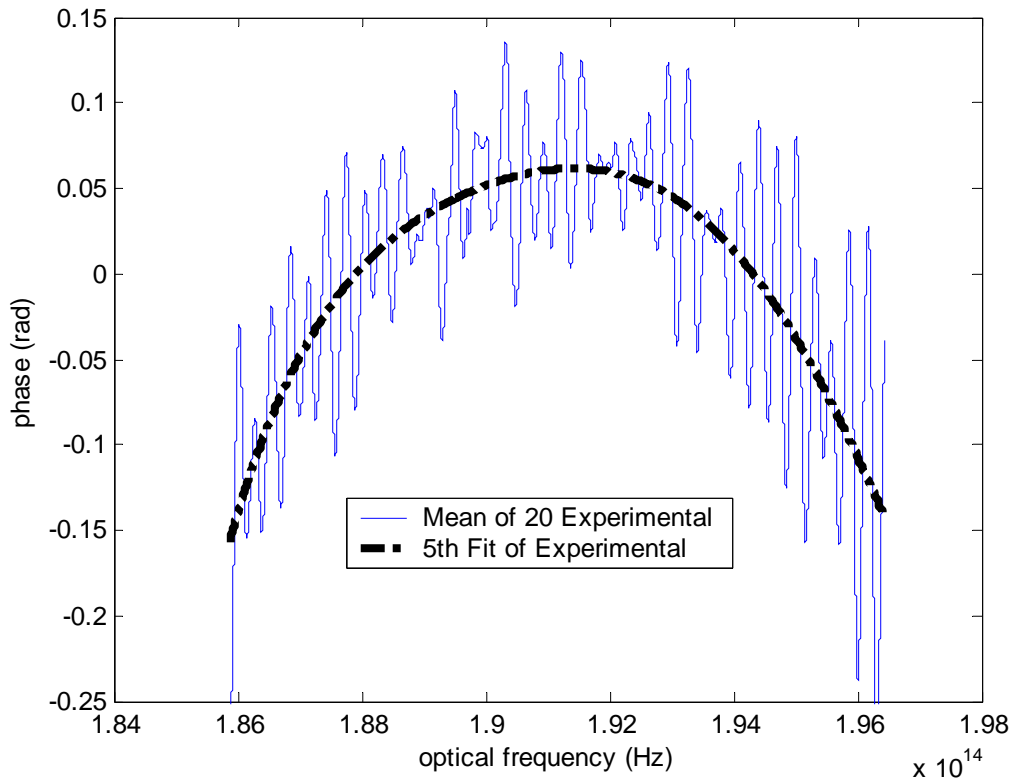


Figure 4.7. Experimentally measured spectral phase variation. Mean of 20 experimental measurements (solid) and 5th order polynomial curve fitting of the mean (dashed).

order polynomial curve fit of the mean.

To verify this method of determining the higher-order refractive index of the test material, this study utilizes a published data set of the refractive index of water, which is estimated from water absorption spectra and Kramers-Kronig transformation by Bertie [4.34, 4.35]. The refractive index of water data is applied to Equation 4.4, and the spectral phase function in Equation 4.17 is calculated and displayed in Figure 4.8. The thin solid line in Figure 4.8 is the spectral phase function of the higher-order refractive index, and

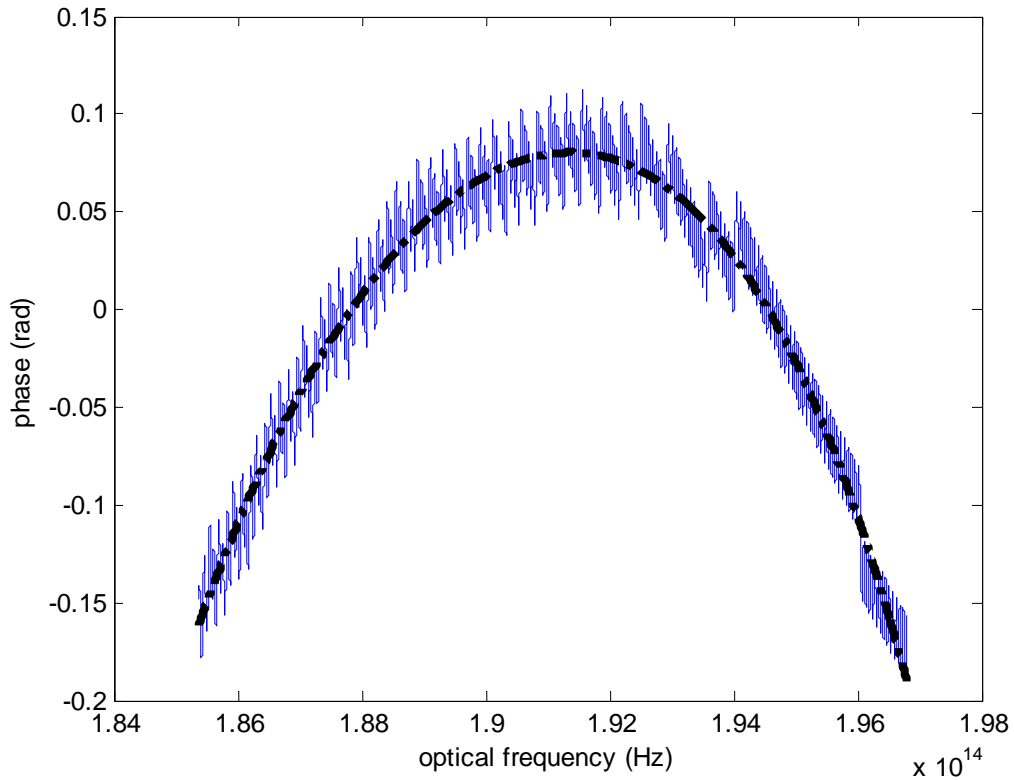


Figure 4.8. Spectral phase variation of refractive index of water estimated by numerical calculation using published water refractive index (solid), 5th order polynomial curve fitting (dashed).

the thick dashed line is the 5th order polynomial curve fitting of the spectral phase function.

Figure 4.9 provides comparison between the two results; the 5th order polynomial curve fit on experimental measurement and numerical calculation utilizing the refractive index of water. The correlation coefficient between the two results is 0.9951, and normalized mean square error is 0.0020. In addition, magnitudes of both results within

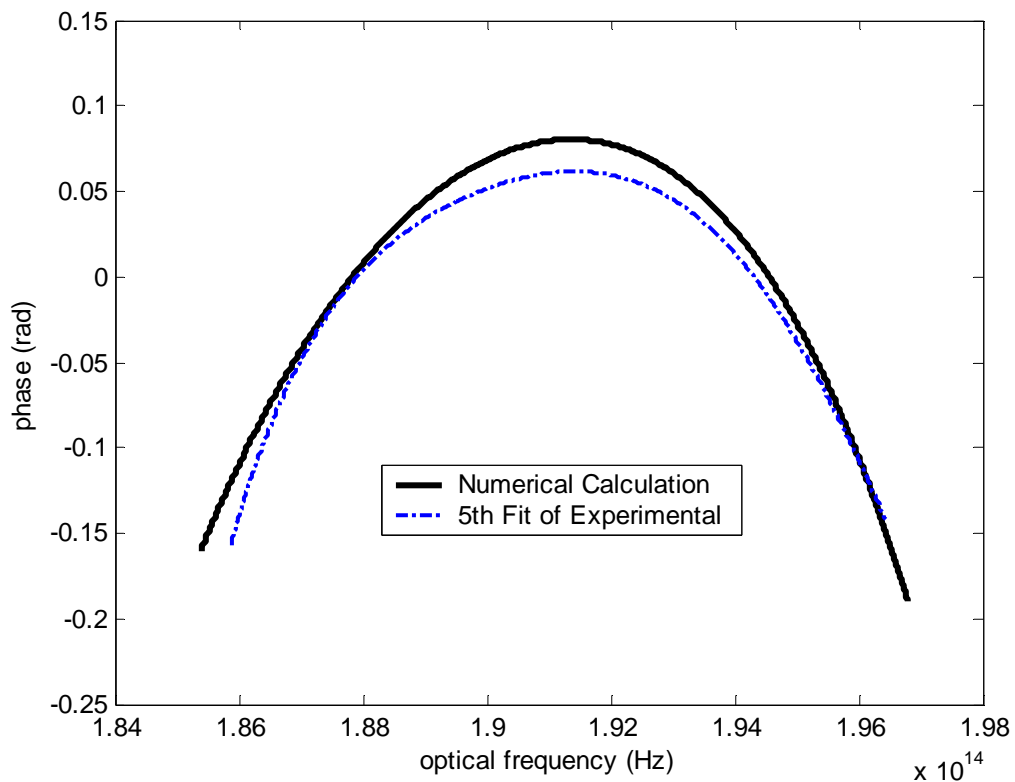


Figure 4.9. Comparison of the two results; 5th order polynomial curve fits of experimental result (dashed) and numerical calculation (solid). Correlation coefficient = 0.995, Normalized mean square error = 0.002.

the optical frequency range are 0.229 rad and 0.219 rad for Bertie and experimental data, respectively.

Figure 4.10-(a) and 4.10-(b) shows the result of the slope of $\varphi_\alpha(\nu) - \varphi_\beta(\nu)$ versus various glucose concentrations in a micro-range and a macro-range, respectively. Each concentration has 20 experimental measurements, and error-bars represent the standard deviation. The dotted line is a linear regression of measured data ($\hat{Y} = 1.7843 \times 10^{-5} \hat{X} + 0.11276$). Correlation coefficients and sensitivities based on root mean square error of prediction (RMSEP) for both ranges are given in Table 4.1.

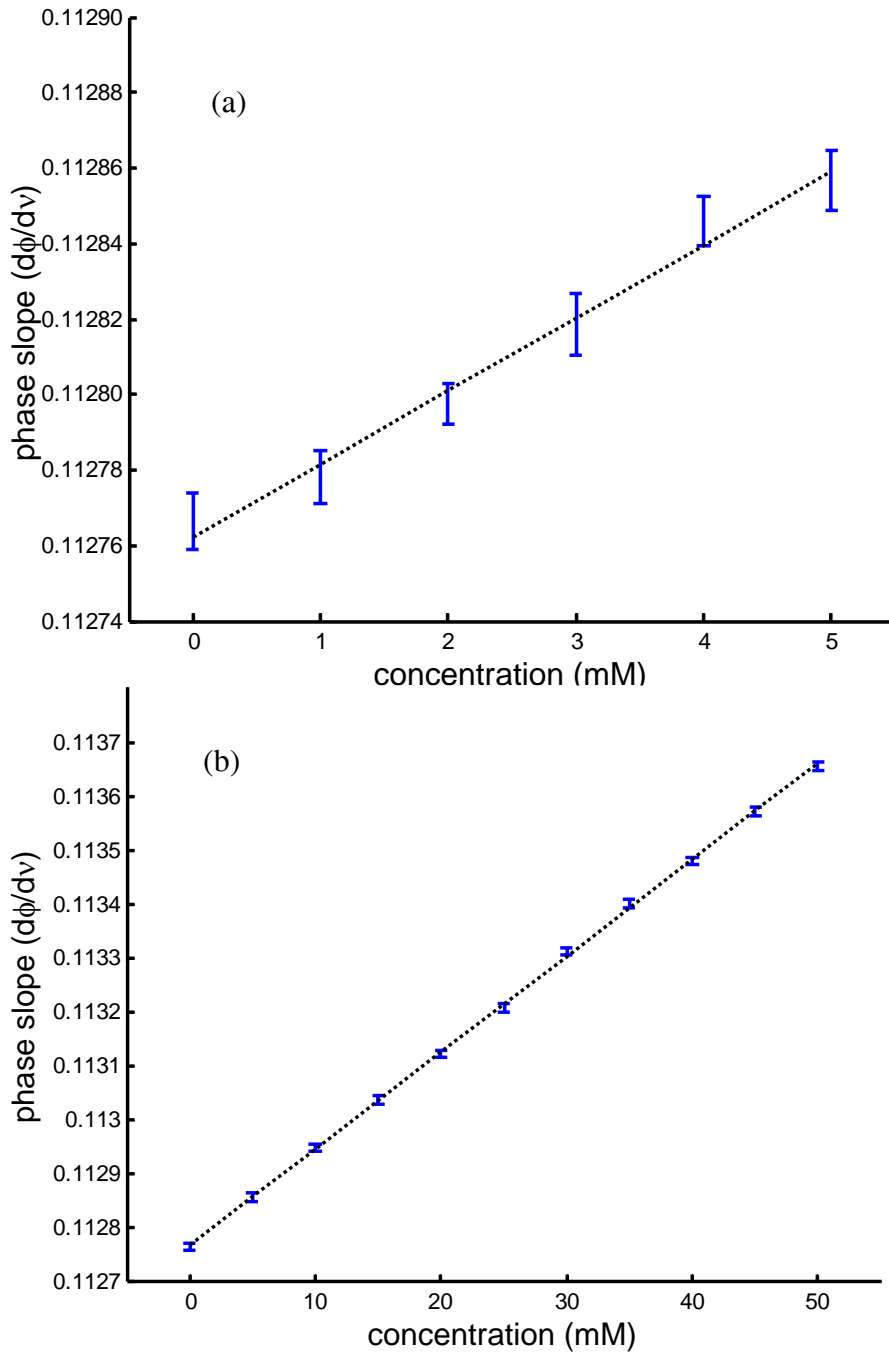


Figure 4.10. Glucose concentration measurement for 0-5 mM in 1 mM increments (a) and 0-50 mM in 5 mM increments (b). Each error-bar represents the standard deviation of 20 measurements.

	Correlation coefficient	Resolution
Micro-range	0.993	0.86 mM
Macro-range	0.999	0.54 mM

Table 4.1. Correlation coefficients and resolutions

4.4. DISCUSSION

Because a portion of light input is absorbed by the water, it is necessary that the path length of water should be short enough to have light reflection passing through it. The inner diameter of the water chamber is as thin as 0.789 mm and wall thickness is 1 mm. Use of a common-path spectral interferometer (SI) provides a common reference and sample path. From a theoretical point of view, one surface of the water chamber can act as a reference reflector for interfering light reflected from the other surface. In this approach, the diminutive dimension of the water chamber results in the location of interference fringes near DC where noise is highest. An additional reference plate positioned several tens of millimeters in front of the sample is utilized so that locations of interference fringes of interest are positioned in a low noise region.

Discovering the optimized combination of weights in the multitaper spectral analysis requires substantial processing time and complexity due to adaptive and stochastic procedures. On the other hand, multitaper spectral analysis affords less side-lobe contamination and maintains a stable spectral estimation. The fast Lomb-Scargle algorithm is an excellent solution for time-frequency transformation with unevenly spaced sample data and provides higher accuracy and less spectral leakage than conventional NUFTs. Moreover, the fast Lomb-Scargle algorithm reduces calculation complexity from $O(N^2)$ to $O(N \log N)$.

According to the comparison between the experimental and numerical results in Figure 4.9, the high correlation coefficient ($\rho = 0.9951$) and low normalized mean squared error (NMSE = 0.0020) indicate excellent agreement between the two results.

The slight difference between the two results may be due to two reasons; non uniform reflection spectra from the water chamber wall and/or experimental error. The data graph of the mean of 20 measurements in Figure 4.7 includes background spectral noise representing subtle fluctuation ranging about 0.1 radian; the numerical result in Figure 4.8 also shows similar noise but with less magnitude. One limitation of this method is that optical frequency range for this analysis is limited by the bandwidth of the swept laser source.

According to Figure 4.10-(a), Figure 4.10-(b), and Table 4.1, the results are highly correlated to the linear regression (correlation coefficient 0.999) and show excellent resolution up to 0.54 mM which is better than previous reports. The micro-range data presents slightly less resolution and accuracy than that in the macro-range; an anticipated reason for this is slight error on sample preparation, but it still demonstrates capability of this method to determine small changes in concentration of glucose solutions. Furthermore, other swept-sources with broader optical-frequency range will improve the resolution and accuracy.

4.5. CONCLUSION

A novel spectral interferometer (SI) and unique data processing procedure are introduced to measure higher-order refractive index and to estimate material dispersion of a target sample. In short, the SI system incorporating a fiber-based common-path interferometer and a high-resolution broad-band frequency swept laser provides a compact, stable experimental system requiring less time and effort in optical construction and makes automatic compensation of dispersion and phase off-set in the system. A unique data processing procedure, spectral phase analysis, uses a fast Lomb-Scargle algorithm and multitaper spectral analysis to process time-frequency data.

A fiber-based common-path spectral interferometer with a frequency swept laser and spectral phase analysis are evaluated by comparison between an experimental result and a numerical calculation with published refractive index of water. Result of this method demonstrates excellent agreement in spectral variation with numerical calculation. This novel SI with unique spectral phase analysis can be an adequate method to determine higher-order refractive index and material dispersion of a target sample.

The results of glucose concentration measurement demonstrate high resolution and accuracy; 0.54 mM of resolution and 0.999 of correlation coefficient. As a consequence of this study, swept-source spectral interferometry with spectral phase analysis can be developed to a candidate method for glucose-sensing. For glucose-sensing, further studies should investigate specificity, scattering dispersion in turbid media, and selection of reflecting surfaces in a tissue sample.

The advantage of this compact and stable optical system is it may be utilized in various optical measurements with minor modifications. The data processing method can

be applied to spectral polarimetry, monitoring photo-thermal expansion, swept-source optical coherence tomography, and many more.

We thank Dr K. Larin for the advices regarding preparation of the samples and providing the sample chamber.

4.6. REFERENCES

- [4.1] Wolf E, Three-dimensional structure determination of semi-transparent objects from holographic data, *Optics Communications*, **1**(4), 153-156, 1969.
- [4.2] Wolf E, Determination of the amplitude and the phase of scattered fields by holography, *Journal of the Optical Society of America*, **60**(1), 18-20, 1970.
- [4.3] Marlow WC, Hakenmethod, *Applied Optics*, **6**(10), 1715-1724, 1967.
- [4.4] Panasenko D, Putilin S, Fainman Y, Tunable spectral interferometry for broadband phase detection by use of a pair of optical parametric amplifiers, *Journal of the Optical Society of America B*, **22**(4), 922-929, 2005.
- [4.5] Likforman J, Joffre M, Thierry-Mieg V, Measurement of photon echoes by use of femtosecond Fourier-transform spectral interferometry, *Optics Letters*, **22**(14), 1104-1106, 1997.
- [4.6] Lepetit L, Cheriaux G, Joffre M, Linear techniques of phase measurement by femtosecond spectral interferometry for applications in spectroscopy, *Journal of the Optical Society of America B*, **12**(12), 2467-2474, 1995.
- [4.7] Hlubina P, Spectral interferometry including the effect of transparent thin films to measure distances and displacements, *Acta Physica Slovaca*, **54**(3), 213-220, 2004.
- [4.8] Fercher AF, Hitzenberger CK, Kamp G, El-Zaiat SY, Measurement of intraocular distances by backscattering spectral interferometry, *Optics Communications*, **117**(1-2), 43-84, 1995.
- [4.9] Kumar VN, Rao DN, Using interference in the frequency domain for precise determination of thickness and refractive indices of normal dispersive materials, *Journal of the Optical Society of America B*, **12**(9), 1559-1563, 1995.
- [4.10] Set SY, Jablonski MK, Hsu K, Goh CS, Rapid amplitude and group-delay measurement system based on intra-cavity-modulated swept-lasers, *IEEE Transactions on Instrumentation and Measurement*, **53**(1), 192-196, 2004.
- [4.11] Costa B, Mazzoni D, Puleo M, Vezzoni E, Phase shift technique for the measurement of chromatic dispersion in optical fibers using LED's, *IEEE Journal of Quantum Electronics*, **30**(10), 1497-1503, 1982.

- [4.12] Ozeki T, Watanabe A, Measurements of wavelength dependence of group delay in a multimode silica fiber, *Applied Physics Letters*, **28**(7), 382-383, 1976.
- [4.13] Dennis T, Williams, PA, Chromatic dispersion measurement error caused by source amplified spontaneous emission, *IEEE Photonics Technology Letters*, **16**(11), 2532-2534, Nov. 2004.
- [4.14] Hammer DX, Welch AJ, Noojin GD, Thomas RJ, Spectrally resolved white-light interferometry for measurement of ocular dispersion, *Journal of the Optical Society of America A*, **16**(9), 2092-2102, 1999.
- [4.15] Calatroni J, Sáinz C, Escalona R, The stationary phase in spectrally resolved white-light interferometry as a refractometry tool, *Journal of Optics A*, **5**, S207-S210, 2003.
- [4.16] Hlubina P, Martynkien T, Urbanczyk W, Dispersion of group and phase modal birefringence in elliptical-core fiber measured by white-light spectral interferometry, *Optics Express*, **11**(22), 2793-2798, 2003.
- [4.17] Wojtkowski M, Srinivasan VJ, Ko TH, Fujimoto JG, Ultrahigh-resolution, high-speed, Fourier domain optical coherence tomography and methods for dispersion compensation, *Optics Express*, **12**(11), 2404-2422, 2004.
- [4.18] Vakhtin AB, Kane DJ, Wood WR, Peterson KA, Common-path interferometer for frequency-domain optical coherence tomography. *Applied Optics*, **42**(34), 6953-6958, 2003.
- [4.19] Vakhtin AB, Peterson KA, Wood WR, Kane, DJ, Differential spectral interferometry: an imaging technique for biomedical applications, *Optics Letters*, **28**(15), 1332-1334, 2003.
- [4.20] Choma MA, Ellerbee AK, Yang C, Creazzo TL, Spectral-domain phase microscopy. *Optics Letters*, **30**(10), 1162-1164, 2005.
- [4.21] Choma MA, Sarunic MV, Yang C, Izatt JA, Sensitivity advantage of swept source and Fourier domain optical coherence tomography, *Optics Express*, **11**(18), 2183-2189, 2003.
- [4.22] Yun SH, Tearney GJ, de Boer JF, Iftimia N, High-speed optical frequency-domain imaging. *Optics Express*, **11**(22), 2953-2963, 2003.
- [4.23] Kim E, Dave D, Milner TE, Fiber-optic spectral polarimeter using a broadband swept laser source, *Optics Communications*, **249**(1-3), 351-356, 2005.

- [4.24] Bruce CF, Ciddor PE, Phase dispersion in multiplayer films, *Journal of the Optical Society of America*, **50**(3), 295-299, 1960.
- [4.25] Lomb NR, Least-squares frequency analysis of unequally spaced data, *Astrophysics and Space Science*, **39**, 447-462, 1976.
- [4.26] Scargle JD, Studies in astronomical time series analysis.II Statistical aspects of spectral analysis of unevenly spaced data, *The Astrophysical Journal*, **263**, 835-853, 1982.
- [4.27] Press WH, Rybicki GB, Fast algorithm for spectral analysis of unevenly sampled data, *The Astrophysical Journal*, **338**, 277-280, 1989.
- [4.28] Thomson DJ, Spectrum estimation and harmonic analysis, *Proceedings of the IEEE*, **70**(9), 1055-1096, 1982.
- [4.29] Slepian D, Prolate spheroidal wave function, Fourier analysis, and uncertainty – V: the discrete case, *Bell Laboratory Technical Journal*, **57**(5), 1371-1430, 1978.
- [4.30] Walden AT, Improved low-frequency decay estimation using the multitaper spectral analysis method, *Geophysical Prospecting*, **38**, 61-86, 1990.
- [4.31] Mellors RJ, Vernon FL, Thomson DJ, Detection of dispersive signals using multitaper dual-frequency coherence, *Geophysical Journal International*, **135**(1), 146-154, 1998.
- [4.32] McCoy EJ, Walden AT, Percival DB, Multitaper spectral estimation of power law processes, *IEEE Transactions on Signal Processing*, **46**(3), 655-668, 1998.
- [4.33] Xu Y, Haykin S, Racine RJ, Multiple window time-frequency distribution and coherence of EEG using Slepian sequences and hermite functions, *IEEE Transactions on Biomedical Engineering*, **46**(7), 861-866, 1999.
- [4.34] Bertie JE, and Lan Z, Infrared Intensities of Liquids XX: The intensity of the OH stretching band of liquid water revisited, and the best current values of the optical constants of H₂O(l) at 25°C between 15,000 and 1 cm⁻¹, *Applied Spectroscopy*, **50**(8), 1047-1057, 1996.
- [4.35] Bertie JE, Lan Z, The refractive index of colorless liquids in the visible and infrared: contributions from the absorption of infrared and ultraviolet radiation and the electronic molar polarizability below 20,500 cm⁻¹, *Journal of Chemical Physics*, **103**(23), 10152-10161, 1995.
- [4.36] McNichols RJ and Coté GL, Optical glucose sensing in biological fluids: an overview, *Journal of Biomedical Optics*, **5**(1), 5-16, 2000.

- [4.37] Yoon G, Amerov AK, Jeon KJ, and Kim YJ, Determination of glucose concentration in a scattering medium based on selected wavelengths by use of an overtone absorption band, *Applied Optics*, **41**(7), 1469-1475, 2002.
- [4.38] Robinson MR, Eaton RP, Haaland DM, Koepp GW, Thomas EV, Stallard BR, and Robinson PL, Noninvasive glucose monitoring in diabetic patients: a preliminary evaluation, *Clinical Chemistry*, **38**(9), 1618-1622, 1992.
- [4.39] Berger AJ, Itzkan I, Feld MS, Feasibility of measuring blood glucose concentration by near-infrared Raman spectroscopy, *Spectrochimica Acta A*, **53**(2), 287-92, 1997.
- [4.40] Wang SY, Hasty CE, Watson PA, Wicksted JP, Stith RD, and March WF, Analysis of metabolites in aqueous solutions by using laser Raman spectroscopy, *Applied Optics*, **32**(6), 925-929, 1993.
- [4.41] Goetz MJ Jr., Coté GL, Erckens R, March WF, and Motamedi M, Application of a multivariate technique to Raman spectra for quantification of body chemicals, *IEEE Transactions on Biomedical Engineering*, **42**(7), 728-731, 1995.
- [4.42] Dou X, Yamaguchi Y, Yamamoto H, Doi S, Ozaki Y, A highly sensitive, compact Raman system without a spectrometer for quantitative analysis of biological samples, *Vibrational Spectroscopy*, **14**(2), 199-205, 1997.
- [4.43] King TW, Coté GL, McNichols R, Goetz MJ Jr., Multispectral polarimetric glucose detection using a single pockels cell, *Optical Engineering*, **33**(8), 2746-2753, 1994.
- [4.44] Cameron BD and Coté GL, Noninvasive glucose sensing utilizing a digital closed-loop polarimetric approach, *IEEE Transactions on Biomedical Engineering*, **44**(12), 1221-1227, 1997.
- [4.45] Coté GL and Cameron BD, Noninvasive polarimetric measurement of glucose in cell culture media, *Journal of Biomedical Optics*, **2**(3), 275-281, 1997.
- [4.46] Feng C, Huang Y, Chang J, Chang M, Chou C, A true phase sensitive optical heterodyne polarimeter on glucose concentration measurement, *Optics Communications*, **141**, 314-321, 1997.
- [4.47] Lakowicz JR, and Maliwal B, Optical sensing of glucose using phase-modulation fluorimetry, *Analytica Chimica Acta*, **271**(1), 155-164, 1993.
- [4.48] Li L and Walt DR, DuallAnalyte Fiberloptic Sensor for the Simultaneous and Continuous Measurement of Glucose and Oxygen, *Analytical Chemistry*, **67**(20), 3746-3752, 1995.

- [4.49] Chen K, Hsu C, and Su D, Interferometric optical sensor for measuring glucose concentration, *Applied Optics*, **42**(28), 5774-5776, 2003.
- [4.50] Nakamura A, Hasegawa T, Nishijo J, Kanazawa M, Aizawa K, and Sota T, Spectroscopic Evaluation of Glucose Concentration in Phosphate-Buffered Saline Solution Using Principal Component Analysis, *Japan Journal of Applied Physics*, **41**-2(4B), L 440–L 442, 2002.
- [4.51] Esenaliev RO, Larin KV, Larina IV, and Motamedi M, Noninvasive monitoring of glucose concentration with optical coherence tomography, *Optics Letters*, **26**(13), 992-994, 2001.
- [4.52] Larin KV, Motamedi M, Ashitkov TV, and Esenaliev RO, Specificity of noninvasive blood glucose sensing using optical coherence tomography technique: a pilot study, *Physics in Medicine and Biology*, **48**, 1371–1390, 2003.
- [4.53] Larin KV, Akkin T, Esenaliev RO, Motamedi M, and Milner TE, Phase-sensitive optical low-coherence reflectometry for the detection of analyte concentrations, *Applied Optics*, **43**(17), 3408-3414, 2004.

Chapter 5: Summary and Conclusions

5.1. SUMMARY OF DISSERTATION

A theoretical view of optical imaging and motivation for dispersion research are described in the first chapter of this dissertation. Next, Chapter 2 reports on work to construct a dispersion control system using a spatial light modulator (SLM) in conjunction with time domain optical coherence tomography (OCT). To test feasibility of the dispersion control system, we measure the group delay by water, analyze phase of the coherence function, and compute the dispersion compensating function of the SLM. Measured result is compared to a numerical simulation result. In addition, a unique interferometer configuration as shown in Figure 2.4 utilizing the SLM is described. We verify that dispersion information in optical coherence imaging can be measured by phase analysis of coherence function in the optical frequency domain and modified for a variety of applications using the control system.

A method to calibrate a SLM is essential to control the dispersion control system for optical imaging described in Chapter 2 is reported in Chapter 3. A differential phase OCT system utilized in this method provides extremely high sensitivity (5.2 nm) which satisfies the requirement to measure phase response by the smallest increment of SLM control. The results demonstrate that the method is suitable to calibrate not only the SLM but also optoelectronic parts which control small difference in optical path length.

Chapter 4 introduces a new concept for using dispersion; utilize material dispersion as useful information to identify or characterize materials similar to conventional absorption and transmission spectroscopy. To measure dispersion, a spectral interferometer and spectral phase analysis techniques are applied. The spectral interferometer analogous to spectral domain OCT includes a fiber-based common-path interferometer and high-resolution broad-band frequency swept laser, and the spectral phase analysis incorporates a generalized Lomb-Scargle periodogram and multitaper spectral analysis. To verify the instrument and analysis, dispersion of water is compared to numerical results using published values of the refractive index of water. The comparison shows excellent agreement in spectral variation. Correlation coefficient (0.995) and normalized mean square error (0.002) are given. Moreover, the fast Lomb-Scargle algorithm reduces calculation complexity from $O(N^2)$ to $O(N \log N)$.

Also, Chapter 4 shows a useful application to measure quantitatively glucose concentration by use of the spectral interferometer and spectral phase analysis. For the experimental use, glucose solutions are prepared in the range of 0-50 mM with 5 mM increment and 1 mM increment in 0-5 mM. The linear regression of recorded data is $\hat{Y} = 1.7843 \times 10^{-5} \hat{X} + 0.11276$. The results demonstrate 0.999 of correlation coefficient and 0.54 mM resolution. These results verify that spectral interferometry with spectral phase analysis is a reliable method to quantitatively determine glucose concentration with excellent resolution and accuracy.

5.2. CONCLUSIONS

This dissertation introduces an alternative viewpoint of material dispersion: utilization to characterize materials. Unique configurations of optical imaging systems are introduced and novel data processing - spectral phase analysis - is utilized to estimate dispersion. Results and discussions conclude that characterizing material dispersion is valuable to characterize the target material and the proposed optical imaging systems and spectral phase analysis are adequate to estimate dispersion.

For future direction of this research, scattering dispersion arising from a turbid media should be considered. A non-homogeneous scattering sample produces scattering dispersion which carries dimensional information. For example, in tissue samples, scattering dispersion may provide size of cells and nuclei. Cancer screening might be facilitated by estimating the size of cells and nuclei using scattering dispersion analysis. The optical system to measure dispersion of homogeneous samples should be modified to give a smaller beam diameter in the sample path, and spectral phase analysis should incorporate scattering theory.

Chapter 6: Future work – Optical Imaging and Characterization of Cancer Cells using Spectral Domain Optical Coherence Tomography for early Cancer Diagnosis.

6.1. INTRODUCTION

Cancer is the second leading cause of human death, exceeded only by heart disease; the American Cancer Society has reported 1,372,910 new cancer cases and 570,280 deaths of cancer patients are expected in the United States in 2005 ^[6.1]. Compared to the 1950's death rate by cause, current death rate for heart and cerebrovascular disease has reduced by 60 % and 70%, respectively, while that for cancer is unchanged. According to the Surveillance, Epidemiology, and End Results (SEER) of Cancer Statistics Review, early cancer diagnosis reduces mortality and morbidity and increases survival rate ^[6.2].

Based on these findings, numerous cancer research efforts have been undertaken to facilitate early cancer diagnosis using modern science and technologies. Over the last two decades, optical spectroscopy and optical imaging technologies have advanced dramatically and emerged as a valuable modality for biological research and potential for cancer diagnosis ^[6.3-6.6]. Optical coherence tomography (OCT) ^[6.7] has potential to improve cancer screening and diagnosis. Optical properties of cancer cells have been studied using OCT. Escobar reported that cancer cells have a difference in light reflection and absorption ^[6.5], and Rylander found a difference in mass and volume between normal

cells and cancer cells utilizing phase sensitive OCT images ^[6.6]. Advanced OCT methods may offer important advantages for clinical research and diagnosis. For instance, polarization sensitive OCT is being investigated for early screening of glaucoma in ophthalmology ^[6.8,6.9], and endoscopic OCT is employed for *in-vivo* cardiovascular imaging ^[6.10, 6.11].

I propose a research plan to develop methods and procedures for early cancer screening and diagnosis, this include design, construction and demonstration of a system that may be utilized for optical imaging and optical spectroscopy. The imaging system will be used to establish a database containing optical properties of cancer and normal cells. The two modes of operation of the imaging system are introduced with preliminary results in “6.2 Methods”, and contributions and applications to cancer research are discussed in “6.3 Expected Results and Discussion.”

6.2. METHODS

I propose to design, construct and demonstrate an imaging system that can produce high-resolution images of the subcellular structure of cancerous lesions and provide spectroscopic characteristics of cancer cells. The imaging system can operate in two modes and combines a spatially multiplexed swept source OCT and spectroscopic OCT. Utilization of the imaging system to establish an information database of normal and cancer cells will provide a valuable resource for advancing optical-based cancer diagnostic techniques.

6.2.1. The First Mode: Spatially Multiplexed Swept Source Optical Coherence Tomography

As the first mode of the imaging system, a spatially multiplexed swept source optical coherence tomography (SMSS-OCT) utilizes a broad-band frequency swept laser which provides extremely narrow line widths (150 KHz) and allows scan lengths on the order of meters in optical depth. The principle of SMSS-OCT is multiplexing the excessively long depth scan into a laterally adjacent B-scan with an appropriate length of depth scan. In other words, the broad-band frequency is spatially distributed in sequence to shorten the scan range in depth. Figure 6.1 illustrates the imaging principles of SMSS-OCT. Figure 6.1-(a) depicts a full scan on one position without any lateral movement which has a long depth scan, while Figure 6.1-(b) shows a spatially multiplexed scan with same light source but a sequentially distributed by lateral movement.

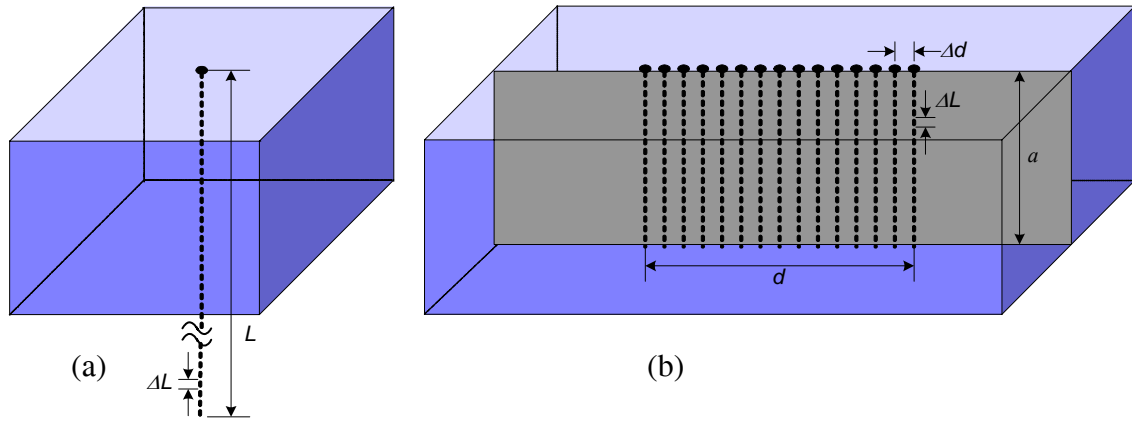


Figure 6.1. Illustration of SMSS-OCT principle: multiplexing excessively long depth scan (a) into a laterally adjacent B-scans (b). L : maximum scan depth, ΔL : longitudinal resolution, Δd : lateral resolution, a : scan depth, d : lateral scan range.

To design a spatially multiplexed two-dimensional imaging system with a frequency swept laser, several parameters should be considered. At first, as shown in Figure 6.1, ΔL is the longitudinal resolution computed by the band width of the light source, therefore the maximum scan depth, L , is calculated by multiplying ΔL by the total number of frequencies, N . Secondly, the scan depth, a , needs to be estimated to be as long as the imaging depth required, and then the number of frequencies, N_a , for each A-scan can be derived by dividing the scan depth by ΔL . Finally, the lateral scan range, d , is computed by multiplying the lateral resolution, Δd , to the number of A-scans, N_d . The number of A-scans is N over N_a . Finally a and d determine the imaging range as shown in the Equation 6.1.

$$L = N \times \Delta L, \quad N = N_a \times N_d, \quad a = N_a \times \Delta L, \quad d = N_d \times \Delta d \quad (6.1)$$

An overall system diagram of the first mode of the imaging system, SMSS-OCT, is depicted in Figure 6.2. The SMSS-OCT system is constructed similar to a fiber-based Michelson type interferometer. It consists of a frequency-swept light source, a photodetector, an analog-to-digital converter (ADC), a workstation computer, a beam splitter, two collimators, a mirror mounted on a Galvanometer, a dichroic mirror, and a sample stage. Input light passes the beam splitter and collimator in the sample path, and then is spatially distributed on the sample for two-dimensional scanning by tilting the mirror mounted on the Galvanometer. The interference signal is coupled into the photodetector and stored in the workstation computer through the ADC.

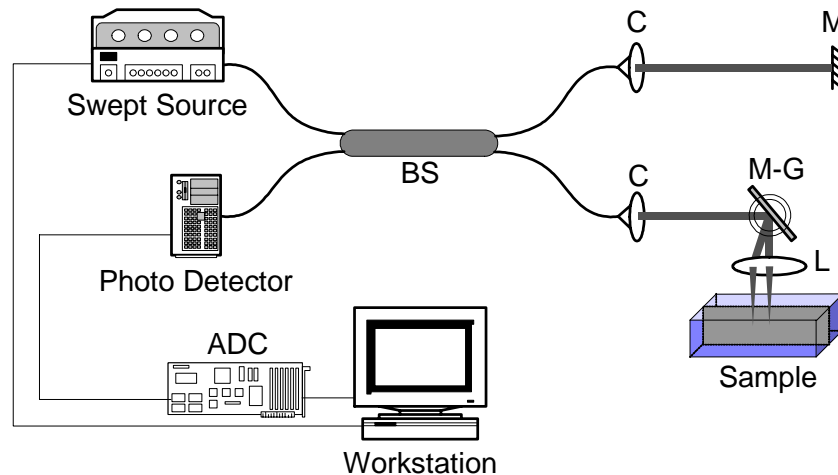


Figure 6.2. System diagram of SMSS-OCT imaging system. BS: beam splitter, C: collimator, M: mirror, M-G: mirror on the galvanometer, L: lens, and ADC: analog to digital converter.

The raw data from the system needs to be processed by a time-frequency transformation to convert the frequency domain data to the time domain data. Because the frequency interval is not equally sampled, a non-uniform Fourier transformation (NUFT) is to the raw data for the time-frequency transformation.

Figure 6.3 displays an image from the SMSS-OCT system. The horizontal axis is the longitudinal depth, and the vertical axis is the stack of A-scans. The depth resolution is 12.4 μm . The sample is a microscope cover slide of 100 μm thickness glass. As Figure 6.3 shows, this imaging system provides a cross-sectional lateral view of the sample. The two white vertical lines represent the front and back surface of the cover slide.

According to this preliminary research on SMSS-OCT, high-resolution sub-

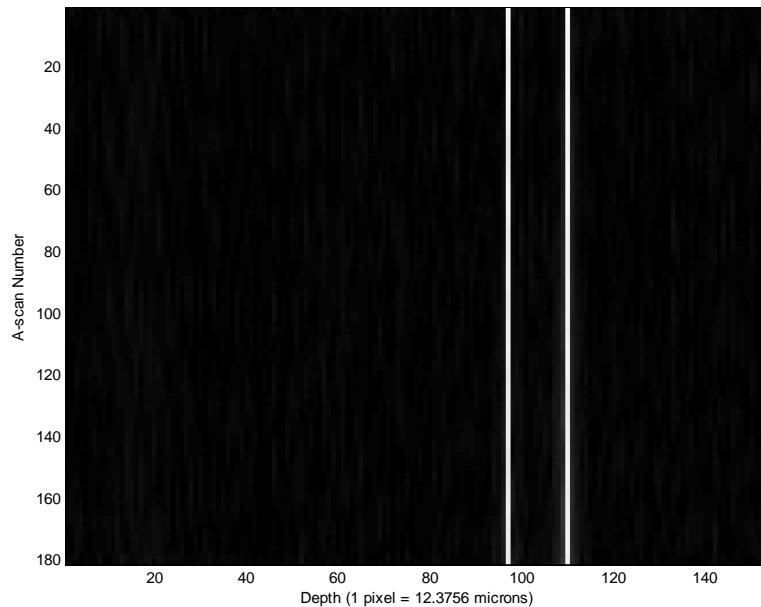


Figure 6.3. SMSS-OCT image of microscope cover slide; glass, 100 μm thickness, $n=1.5$

cellular images from this system allow one to visualize cancerous lesions and localize the cancer cells. This imaging modality with an appropriate light source promises to improve image quality and clinical accuracy. Once suspicious cells are localized by the first mode of the imaging system, the cells can be analyzed by the second mode, a spectroscopic OCT which can provide the optical characteristics of the cells, for example, cell volume, refractive index, and material dispersion.

6.2.2. The second mode: Spectroscopic Optical Coherence Tomography

Spectroscopic OCT is a modern electro-optical system that can measure spectroscopic dependent data of a sample. Overall system diagram is displayed in Figure 6.4. A spectroscopic OCT system is comprised of a broad-band frequency swept laser, a photodetector, an ACD, computer workstation, circulator, collimator, reference glass plate, lens, and sample chamber. The light source is a broad-band frequency swept laser. Input light from the light source passes the circulator and collimator. Light is reflected from the reference and each surface of the sample chamber which is a cuvette. Each reflected light beam interferes, and is detected by the photodetector after passing the

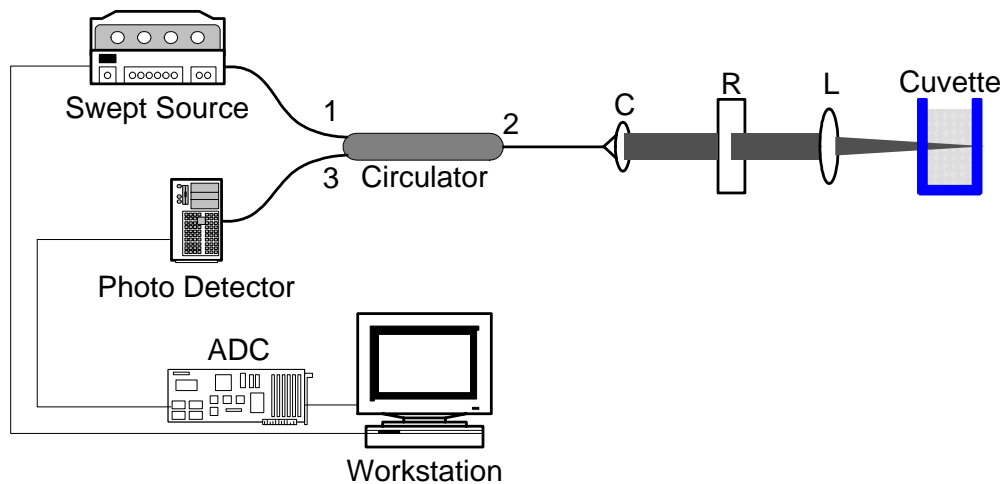


Figure 6.4. Second mode; spectroscopic OCT imaging system. C: collimator, R: reference glass plate, M-G: mirror on the galvanometer, L: lens, and ADC: analog to digital converter.

circulator. Finally, the detected signal is stored in the computer workstation. This system has a common path rather than a separated reference and sample path. The advantages of a common path are simplified optical construction, convenience of system alignment, and phase stability.

After a couple of signal processing procedures, the measured raw data is converted to highly sensitive spectral phase data, which can give important optical characteristics of the sample, including material dispersion and refractive index variation. This spectral phase analysis can be used as a method to discriminate abnormal

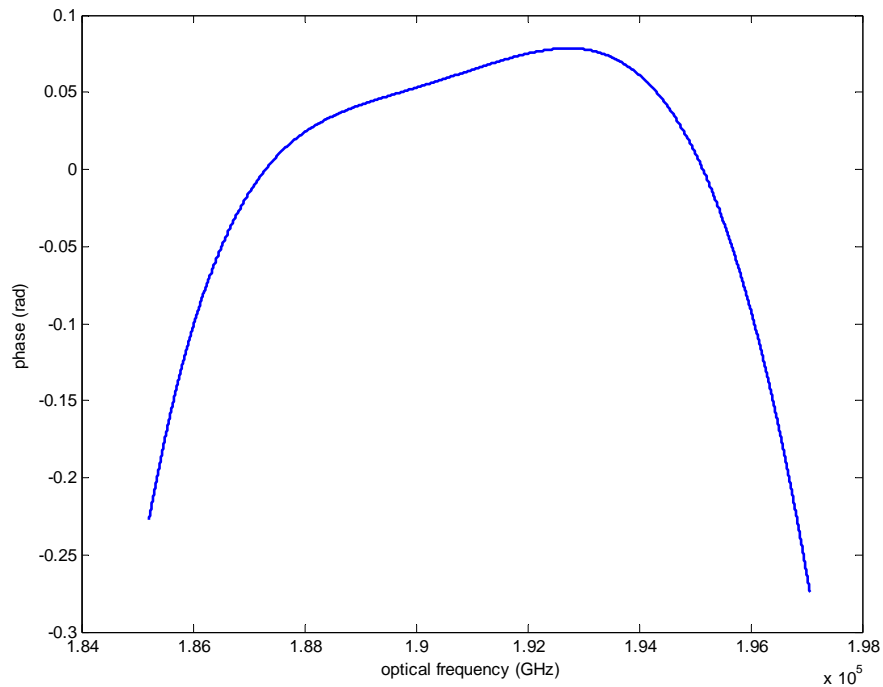


Figure 6.5. High-order spectral phase variation of water (H₂O)

characteristics from normal. Figure 6.5 shows the spectroscopic phase data of water (H_2O) measured from spectroscopic OCT described above. The horizontal axis is optical frequency in GHz, and the vertical axis is phase in radians. The linear and constant parts of the phase function are excluded to show only the high-order phase variation. This experimental result is well matched to the numerical simulation using the water refractive index. This high-order phase variation is closely related to material dispersion which is one of the important characteristics used to identify the structure and constituent of the material. Therefore, this method can provide critical factors to discriminate specific cells, for instance cancer and tumor, from normal cells.

With these two modern optical modalities and their databases, we propose an innovative clinical procedure to perform early cancer screening and diagnosis. At the first clinical procedure, the first mode of the imaging system, SMSS-OCT, provides high-resolution sub-cellular images for seeking suspicious lesions such as containing cancer cells. If a suspicious lesion is found from the first procedure, then the second clinical procedure performs a highly sensitive spectral phase analysis using the second mode of the imaging system functioning spectroscopic OCT on the suspicious lesion. Result of the second clinical procedure is assessed by the database of optical characteristics for cancer and normal cells. Finally, the suspicious lesion would be diagnosed as either cancer or normal.

For convenient clinical research the two OCT modalities may be combined into one system. Both modalities have the same components except the beam splitter and the reference mirror on the SMSS-OCT and the circulator on the spectral OCT. Also, the reference path in the SMSS-OCT can be eliminated by employing a common path similar to the spectral OCT. To switch one mode to the other, the control program in the

workstation computer alters the movement of the galvanometer without any optical construction change.

6.3. EXPECTED RESULTS AND DISCUSSION

The two modes of the imaging system, SMSS-OCT and spectroscopic OCT are proposed and introduced, and their preliminary results are reviewed and discussed. The results verify that combination of these two optical modalities will be a promising method to promote the accuracy of early cancer diagnosis, and consequently the method helps to reduce mortality and morbidity of the cancer patient. Because both systems are operated *in-vivo* and are non-invasive, they will be convenient and useful in clinical research. In addition, the two modalities are unified in their similarity, and consequently this system will be more convenient and reduce cost and complexity of construction.

Comparing to traditional OCT system for two-dimensional imaging, the first mode of the imaging system, SMSS-OCT, does not require any optical path length change or lateral movement of the sample. It uses a unique concept of spatial multiplexing implementing a narrow line width broad-band frequency swept laser. Even though the optical construction of SMSS-OCT is fairly simple, it shows excellent performance in imaging. The image out put from this modality provides high-resolution sub-cellular images which is clear enough to recognize a suspicious cancerous lesion.

The second mode of the imaging system, spectroscopic OCT, gives several significant functions to discriminate certain types of material. It provides a spectral phase function which can be rudimentary to estimate refractive index and dispersion. Also, scattering dispersion analysis is possible available employing a scattering theory. These outstanding functions will provide a powerful ability to achieve early cancer diagnosis successfully. Furthermore, these optical modalities can be implemented to a fiber-based design and microstructure in order to be applicable to an *in-vivo* endoscopic system. This

proposed optical imaging system and method will be an excellent research project to improve clinical research dramatically in early cancer screening and diagnosis.

6.4. REFERENCES

- [6.1] American Cancer Society, *Cancer Facts & Figures 2005*, American Cancer Society Inc., No. 5008.05, Atlanta, GA, 2005.
- [6.2] Ries LAG, Eisner MP, Kosary CL, Hankey BF, Miller BA, Clegg L, Mariotto A, Feuer EJ, Edwards BK (eds). *SEER Cancer Statistics Review, 1975-2002*, National Cancer Institute. Bethesda, MD, http://seer.cancer.gov/csr/1975_2002/, based on November 2004 SEER data submission, posted to the SEER web site, 2005.
- [6.3] Mahadevan-Jansen A, Mitchell MF, Ramanujam N, Malpica A, Thomsen S, Utzinger U, Richards-Kortum R, Near-infrared Raman spectroscopy for in vitro detection of cervical precancers, *Photochemistry and Photobiology*, **68**(1), 123-132, 1998.
- [6.4] Gillenwater A, Jacob R. Richards-Kortum R, Fluorescence spectroscopy: a technique with a potential to improve the early detection of aerodigestive tract neoplasia, *Head and Neck*, **20**(6), 556-562, 1998.
- [6.5] Escobar PF; Belinson JL; White A; Shakhova NM; Feldchtein FI; Kareta MV; Gladkova ND., Diagnostic efficacy of optical coherence tomography in the management of preinvasive and invasive cancer of uterine cervix and vulva, *International Journal of Gynecological Cancer*, **14** (3), 470-474, 2004.
- [6.6] Rylander CG, Davé DP, Milner TE, Diller KR, and Welch AJ, Measurement of Total Cell Dry Mass using Differential Phase Contrast Optical Coherence Microscopy (DPC-OCM) to Discriminate Normal and Cancerous Cell Populations, *Cancer Detection and Prevention*, 2005 (in processing).
- [6.7] Huang D, Swanson EA, Lin CP, Schuman JS, Stinson WG, Chang W, Hee MR, Flotte T, Gregory K, Puliafito CA, and Fujimoto JG, Optical coherence tomography, *Science*, **254**, 1178-1181, 1991.
- [6.8] Wollstein G; Schuman JS; Price LL; Aydin A; Stark PC; Hertzmark E; Lai E; Ishikawa H; Mattox C; Fujimoto JG; Paunescu LA, Optical coherence tomography longitudinal evaluation of retinal nerve fiber layer thickness in glaucoma, *Archives of Ophthalmology*, **123**(4), 464-70, 2005.
- [6.9] Kemp NJ, Park J, Zaatari HN, Rylander HG, High-sensitivity determination of birefringence in turbid media with enhanced polarization-sensitive optical

- coherence tomography, *Journal of the Optical Society of America A*, **22**(3), 552-60, 2005.
- [6.10] Fujimoto JG; Boppart SA; Tearney GJ; Bouma BE; Pitris C; Brezinski ME, High resolution in vivo intra-arterial imaging with optical coherence tomography, *Heart*, **82**(2), 128-33, 1999.
- [6.11] Yabushita H, Bouma BE, Houser SL, Aretz HT, Jang I, Schlendorf KH, Kauffman KR, Shishkov M, Kang D, Halpern EF, and Tearney GJ, Characterization of Human Atherosclerosis by Optical Coherence Tomography, *Circulation*, **106**, 1640-1645, 2002.

Glossary

ADC - Analog-to-digital converter

DC - Direct current

DFT - Discrete Fourier transformation

DIUF - Deionized ultra high filtered water

DPOCT - Differential phase optical coherence tomography

DPSS - Discrete prolate spheroidal sequence

FFT - Fast Fourier transformation

FWHM - Full width half maximum

GPIB - General Purpose Interface Bus

ID - Inner diameter

NMSE - Normalized mean squared error

NUFT - Non-uniform Fourier transformation

OCT - Optical Coherence Tomography

OPD - Optical path length difference

PM - Polarization maintained

RMSEP - Root mean square error of prediction

RSDL - Rapid scanning delay line

SI - Spectral interferometry

SLM - Spatial Light Modulator

SEER - the Surveillance, Epidemiology, and End Results (of National Cancer Institute)

SMSS-OCT - Spatially multiplexed swept source optical coherence tomography

STD - Standard deviation

USB - Universal serial bus

Bibliography

Alphabetized List

- [1] Akkin T, Dave DP, Thomas EM, and Rylander HG III, Detection of neural activity using phase-sensitive optical low-coherence reflectometry, *Optics Express*, **12**(1), 2377-2386, 2004.
- [2] American Cancer Society, *Cancer Facts & Figures 2005*, American Cancer Society Inc., No. **5008.05**, Atlanta, GA, 2005.
- [3] Berger AJ, Itzkan I, Feld MS, Feasibility of measuring blood glucose concentration by near-infrared Raman spectroscopy, *Spectrochimica Acta A.*, **53**(2), 287-92, 1997.
- [4] Bergeron A, Gauvin J, Gagnon F, Gingras D, Arsenault HH, and Doucet M. Phase calibration and applications of a liquid-crystal spatial light modulator. *Applied Optics*, **34**(23), 5133-5139, 1995.
- [5] Bertie JE and Lan Z, Infrared Intensities of Liquids XX: The intensity of the OH stretching band of liquid water revisited, and the best current values of the optical constants of H₂O(l) at 25°C between 15,000 and 1 cm⁻¹, *Applied Spectroscopy*, **50**(8), 1047-1057, 1996.
- [6] Bertie JE and Lan Z, The refractive index of colorless liquids in the visible and infrared: contributions from the absorption of infrared and ultraviolet radiation and the electronic molar polarizability below 20500 cm⁻¹, *Journal of Chemical Physics*, **103**(23), 10152-10161, 1995.
- [7] Bordenave E, Abraham E, Jonusauskas G, Tsurumachi N, Oberle J, Rullie`re C, Minot PE, Lasse`gues M, and Bazeille JES, Wide-field optical coherence tomography: imaging of biological tissues, *Applied Optics*, **41**(10), 2059-2064, 2002.
- [8] Born M and Wolf E, *Principal of optics 7th ed.*, p.14-24, Cambridge University Press, Cambridge, 1999.
- [9] Boyde A, Stereoscopic images in confocal (tandem scanning) microscopy, *Science*, **230**(4731), 1270-1272, 1985.

- [10] Brakenhoff GJ, van der Voort HTM, van Spronsen EA, Linnemans WAM, and Nanninga N, Three-dimensional chromatin distribution in neuroblastoma nuclei shown by confocal scanning laser microscopy, *Nature*, **317**, 748-749, 1985.
- [11] Brezinski ME and Fujimoto JG, Optical Coherence Tomography: High-Resolution Imaging in Nontransparent Tissue, *IEEE Journal of selected topics in quantum electronics*, **5**(4), pp.1185-1192, 1999.
- [12] Bruce CF, Ciddor PE, Phase dispersion in multiplayer films, *Journal of the Optical Society of America*, **50**(3), 295-299, 1960.
- [13] Calatroni J, Sáinz C, Escalona R, The stationary phase in spectrally resolved white-light interferometry as a refractometry tool, *Journal of Optics A*, **5**, S207-S210, 2003.
- [14] Cameron BD and Coté GL, Noninvasive glucose sensing utilizing a digital closed-loop polarimetric approach, *IEEE Transactions on Biomedical Engineering*, **44**(12), 1221-1227, 1997.
- [15] Chen K, Hsu C, and Su D, Interferometric optical sensor for measuring glucose concentration, *Applied Optics*, **42**(28), 5774-5776, 2003.
- [16] Choma MA, Ellerbee AK, Yang C, Creazzo TL, Spectral-domain phase microscopy. *Optics Letters*, **30**(10), 1162-1164, 2005.
- [17] Choma MA, Sarunic MV, Yang C, Izatt JA, Sensitivity advantage of swept source and Fourier domain optical coherence tomography, *Optics Express*, **11**(18), 2183-2189, 2003.
- [18] Costa B, Mazzoni D, Puleo M, Vezzoni E, Phase shift technique for the measurement of chromatic dispersion in optical fibers using LED's, *IEEE Journal of Quantum Electronics*, **30**(10), 1497-1503, 1982.
- [19] Coté GL and Cameron BD, Noninvasive polarimetric measurement of glucose in cell culture media, *Journal of Biomedical Optics*, **2**(3), 275-281, 1997.
- [20] Dave DP and Milner TE, Optical low-coherence reflectometer for differential phase measurement. *Optics Letters*, **25**(4), 227-229, 2000.
- [21] Dave DP, Akkin T, Milner TE, and Rylander HG III. Phase-sensitive frequency-multiplexed optical low-coherence reflectometry, *Optics Communications*, **193**, 39-43, 2001.

- [22] DeBoer JF, Cense B, Park BH, Pierce MC, Tearney GJ, and Bouma BE, Improved signal-to-noise ratio in spectral-domain compared with time-domain optical coherence tomography, *Optics Letters*, **28**, 2067-2069, 2003.
- [23] Dennis T, Williams, PA, Chromatic dispersion measurement error caused by source amplified spontaneous emission, *IEEE Photonics Technology Letters*, **16**(11), 2532-2534, Nov. 2004.
- [24] Dou X, Yamaguchi Y, Yamamoto H, Doi S, Ozaki Y, A highly sensitive, compact Raman system without a spectrometer for quantitative analysis of biological samples, *Vibrational Spectroscopy*, **14**(2), 199-205, 1997.
- [25] Escobar PF; Belinson JL; White A; Shakhova NM; Feldchtein FI; Kareta MV; Gladkova ND., Diagnostic efficacy of optical coherence tomography in the management of preinvasive and invasive cancer of uterine cervix and vulva, *International Journal of Gynecological Cancer*, **14** (3), 470-474, 2004.
- [26] Esenaliev RO, Larin KV, Larina IV, and Motamedi M, Noninvasive monitoring of glucose concentration with optical coherence tomography, *Optics Letters*, **26**(13), 992-994, 2001.
- [27] Feng C, Huang Y, Chang J, Chang M, Chou C, A true phase sensitive optical heterodyne polarimeter on glucose concentration measurement, *Optics Communications*, **141**, 314-321, 1997.
- [28] Fercher AF, Drexler W, Hitzenberger CK and Lasser T, Optical coherence tomography—principles and applications, *Reports on Progress in Physics*, **66**, [239-303](#), 2003.
- [29] Fercher AF, Hitzenberger CK, Kamp G, El-Zaiat SY, Measurement of intraocular distances by backscattering spectral interferometry, *Optics Communications*, **117**(1-2), 43-84, 1995.
- [30] Fercher AF, Hitzenberger CK, Sticker M, Zawadzki R, Karamata B, and Lasser T, Dispersion compensation for optical coherence tomography depth-scan signals by a numerical technique, *Optics Communications*, **204**, 67-74, 2002.
- [31] Fercher AF, Hitzenberger CK, Sticker M, Zawadzki R, Karamata B, and Lasser T, Numerical dispersion compensation for Partial Coherence Interferometry and Optical Coherence Tomography, *Optics Express*, **9**(12), 610-615, 2001.
- [32] Fujimoto JG; Boppart SA; Tearney GJ; Bouma BE; Pitris C; Brezinski ME, High resolution in vivo intra-arterial imaging with optical coherence tomography, *Heart*, **82**(2), 128-33, 1999.

- [33] Gillenwater A, Jacob R, Richards-Kortum R, Fluorescence spectroscopy: a technique with a potential to improve the early detection of aerodigestive tract neoplasia, *Head and Neck*, **20**(6), 556-562, 1998.
- [34] Goetz MJ Jr., Coté GL, Erckens R, March WF, and Motamedi M, Application of a multivariate technique to Raman spectra for quantification of body chemicals, *IEEE Transactions on Biomedical Engineering*, **42**(7), 728-731, 1995.
- [35] Hammer DX, Welch AJ, Noojin GD, Thomas RJ, Spectrally resolved white-light interferometry for measurement of ocular dispersion, *Journal of the Optical Society of America A*, **16**(9), 2092-2102, 1999.
- [36] Hammer DX, Welch AJ, Noojin GD, Thomas RJ, Stolarski DJ, and Rockwell BA, Spectrally resolved white-light interferometry for measurement of ocular dispersion, *Journal of Optical Society of America A*, **16**(9), 2092-2102, 1999.
- [37] Hitzenberger CK and Fercher AF, Differential phase contrast in optical coherence tomography, *Optics Letters*, **24**(9), 622-624, 1999.
- [38] Hitzenberger CK, Baumgartner A, Drexler W, and Fercher AF, Dispersion effects in partial coherence interferometry: Implications for intraocular ranging, *Journal of Biomedical Optics*, **4**(1), 144-151, 1999.
- [39] Hlubina P, Martynkien T, Urbanczyk W, Dispersion of group and phase modal birefringence in elliptical-core fiber measured by white-light spectral interferometry, *Optics Express*, **11**(22), 2793-2798, 2003.
- [40] Hlubina P, Spectral interferometry including the effect of transparent thin films to measure distances and displacements, *Acta Physica Slovaca*, **54**(3), 213-220, 2004.
- [41] Huang D, Swanson EA, Lin CP, Schuman JS, Stinson WG, Chang W, Hee MR, Flotte T, Gregory K, Puliafito CA, and Fujimoto JG, Optical coherence tomography, *Science*, **254**(5035), 1178-1181, 1991.
- [42] Kemp NJ, Park J, Zaatari HN, Rylander HG, High-sensitivity determination of birefringence in turbid media with enhanced polarization-sensitive optical coherence tomography, *Journal of the Optical Society of America A*, **22**(3), 552-60, 2005.
- [43] Kim E, Dave D, Milner TE, Fiber-optic spectral polarimeter using a broadband swept laser source, *Optics Communications*, **249**(1-3), 351-356, 2005.

- [44] Kim YL, Walsh JT Jr., and Glucksberg M.R, Phase-slope and group-dispersion calculations in the frequency domain by simple optical low-coherence reflectometry, *Applied Optics*, **42**(34), 6959-6966, 2003.
- [45] King TW, Coté GL, McNichols R, Goetz MJ Jr., Multispectral polarimetric glucose detection using a single pockels cell, *Optical Engineering*, **33**(8), 2746-2753, 1994.
- [46] Knox WH, Pearson NM, Li KD, and Hirlimantt CA, Interferometric measurements of femtosecond group delay in optical components, *Optics Letters*, **13**(7), 574-576, 1988.
- [47] Kratz A and Lewandrowski KB, Case records of the Massachusetts General Hospital, normal reference laboratory values, *The New England Journal of Medicine*, **339**(15), 1063-1072, 1998.
- [48] Kumar VN, Rao DN, Using interference in the frequency domain for precise determination of thickness and refractive indices of normal dispersive materials, *Journal of the Optical Society of America B*, **12**(9), 1559-1563, 1995.
- [49] Lakowicz JR, and Maliwal B, Optical sensing of glucose using phase-modulation fluorimetry, *Analytica Chimica Acta*, **271**(1), 155-164, 1993.
- [50] Larin KV, Akkin T, Esenaliev RO, Motamedi M, and Milner TE, Phase-sensitive optical low-coherence reflectometry for the detection of analyte concentrations, *Applied Optics*, **43**(17), 3408-3414, 2004.
- [51] Larin KV, Motamedi M, Ashitkov TV, and Esenaliev RO, Specificity of noninvasive blood glucose sensing using optical coherence tomography technique: a pilot study, *Physics in Medicine and Biology*, **48**, 1371-1390, 2003.
- [52] Leitgeb R, Hitzengerger CK, and Fercher AF, Performance of Fourier domain vs. time domain optical coherence tomography, *Optics Express*, **11**, 889-894, 2003.
- [53] Lepetit L, Cheriaux G, Joffre M, Linear techniques of phase measurement by femtosecond spectral interferometry for applications in spectroscopy, *Journal of the Optical Society of America B*, **12**(12), 2467-2474, 1995.
- [54] Li L and Walt DR, DualAnalyte Fiberloptic Sensor for the Simultaneous and Continuous Measurement of Glucose and Oxygen, *Analytical Chemistry*, **67**(20), 3746-3752, 1995.

- [55] Likforman J, Joffre M, Thierry-Mieg V, Measurement of photon echoes by use of femtosecond Fourier-transform spectral interferometry, *Optics Letters*, **22**(14), 1104-1106, 1997.
- [56] Lomb NR, Least-squares frequency analysis of unequally spaced data, *Astrophysics and Space Science*, **39**, 447-462, 1976.
- [57] Mahadevan-Jansen A, Mitchell MF, Ramanujam N, Malpica A, Thomsen S, Utzinger U, Richards-Kortum R, Near-infrared Raman spectroscopy for in vitro detection of cervical precancers, *Photochemistry and Photobiology*, **68**(1), 123-132, 1998.
- [58] Marks DL, Oldenburg AL, Reynolds JJ, and Boppart SA, Autofocus algorithm for dispersion correction in optical coherence tomography, *Applied Optics*, **42**(16), 3038-3046, 2003.
- [59] Marlow WC, Hakenmethod, *Applied Optics*, **6**(10), 1715-1724, 1967.
- [60] Martin-Badosa E, Carnicer A, Juvells I, and Vallmitjana S, Complex modulation characterization of liquid crystal devices by interferometric data correction, *Measurement Science and Technology*, **8**(7), 764-772, 1997.
- [61] McCoy EJ, Walden AT, Percival DB, Multitaper spectral estimation of power law processes, *IEEE Transactions on Signal Processing*, **46**(3), 655-668, 1998.
- [62] McNichols RJ and Coté GL, Optical glucose sensing in biological fluids: an overview, *Journal of Biomedical Optics*, **5**(1), 5-16, 2000.
- [63] Mellors RJ, Vernon FL, Thomson DJ, Detection of dispersive signals using multitaper dual-frequency coherence, *Geophysical Journal International*, **135**(1), 146-154, 1998.
- [64] Milner TE, Class Notes of Noninvasive Optical Tomography in Spring 2003, BME389J in the University of Texas at Austin., 2003.
- [65] Mochizuki K. Degree of polarization in jointed fibers: the Lyot depolarizer, *Applied Optics*, **23**(19), 3284-3288, 1984.
- [66] Morgan F, Barbarese E, and Carson JH, Visualizing cells in three dimensions using confocal microscopy, image reconstruction and isosurface rendering: application to glial cells in mouse central nervous system, *Scanning Microscopy*, **6**(2), 345-356, 1992.

- [67] Nakamura A, Hasegawa T, Nishijo J, Kanazawa M, Aizawa K, and Sota T, Spectroscopic Evaluation of Glucose Concentration in Phosphate-Buffered Saline Solution Using Principal Component Analysis, *Japan Journal of Applied Physics*, **41-2(4B)**, L 440–L 442, 2002.
- [68] National Institute of Diabetes and digestive and Kidney Diseases, *Diabetes Overview (DM-119)*, NIH Publication No. **05–3873**, National Institute of Health, 2005.
Web Link <http://diabetes.niddk.nih.gov/dm/pubs/overview/index.htm>
- [69] National Institute of Diabetes and digestive and Kidney Diseases, *Diabetes Control and Complications Trial (DM-162)*, NIH Publication No. **02–3874**, National Institute of Health, 2001.
Web Link <http://diabetes.niddk.nih.gov/dm/pubs/control/index.htm>
- [70] Oh S and Milner TE, A Fiber-based Common-path Spectral Interferometry using a Frequency Swept Laser for Measurement of Refractive Index and Dispersion, *Lasers in Surgery and Medicine*, (submitted in 2006).
- [71] Ozeki T, Watanabe A, Measurements of wavelength dependence of group delay in a multimode silica fiber, *Applied Physics Letters*, **28(7)**, 382-383, 1976.
- [72] Panasenko D, Putilin S, Fainman Y, Tunable spectral interferometry for broadband phase detection by use of a pair of optical parametric amplifiers, *Journal of the Optical Society of America B*, **22(4)**, 922-929, 2005.
- [73] Press WH and Rybicki GB, Fast algorithm for spectral analysis of unevenly sampled data, *The Astrophysical Journal*, **338**, 277-280, 1989.
- [74] Ries LAG, Eisner MP, Kosary CL, Hankey BF, Miller BA, Clegg L, Mariotto A, Feuer EJ, Edwards BK (eds). *SEER Cancer Statistics Review, 1975-2002*, National Cancer Institute. Bethesda, MD,
Web Link http://seer.cancer.gov/csr/1975_2002/, based on November 2004 SEER data submission, posted to the SEER web site, 2005.
- [75] Robinson MR, Eaton RP, Haaland DM, Koepp GW, Thomas EV, Stallard BR, and Robinson PL, Noninvasive glucose monitoring in diabetic patients: a preliminary evaluation, *Clinical Chemistry*, **38(9)**, 1618-1622, 1992.
- [76] Rylander CG, Dave DP, Akkin T, Milner TE, Diller KR, and Welch AJ, Quantitative phase-contrast imaging of cells with phase-sensitive optical coherence microscopy, *Optics Letters*, **29(13)**, 1509-1511, 2004.
- [77] Rylander CG, Davé DP, Milner TE, Diller KR, and Welch AJ, Measurement of Total Cell Dry Mass using Differential Phase Contrast Optical Coherence

Microscopy (DPC-OCM) to Discriminate Normal and Cancerous Cell Populations, *Cancer Detection and Prevention*, 2005 (in processing).

- [78] Scargle JD, Studies in astronomical time series analysis.II Statistical aspects of spectral analysis of unevenly spaced data, *The Astrophysical Journal*, **263**, 835-853, 1982.
- [79] Schmitt JM, Optical Coherence Tomography (OCT): A Review, *IEEE Journal of Selected Topics in Quantum Electronics*, **5**(4), 1205-1215, 1999.
- [80] Set SY, Jablonski MK, Hsu K, Goh CS, Rapid amplitude and group-delay measurement system based on intra-cavity-modulated swept-lasers, *IEEE Transactions on Instrumentation and Measurement*, **53**(1), 192-196, 2004.
- [81] Shirai T, Liquid-crystal adaptive optics based on feedback interferometry for high-resolution retinal imaging, *Applied Optics*, **41**(19), 4013-4023, 2002.
- [82] Slepian D, Prolate spheroidal wave function, Fourier analysis, and uncertainty – V: the discrete case, *Bell Laboratory Technical Journal*, **57**(5), 1371-1430, 1978.
- [83] Sticker M, Hitzenberger CK, Leitgeb R, and Fercher AF, Quantitative differential phase measurement and imaging in transparent and turbid media by optical coherence tomography. *Optics Letters*, **26**(8), 518-520, 2001.
- [84] Suda A, Onish Y, Nagasaka K, Wang P, and Midorikawa K, A spatial light modulator based on fused-silica plates for adaptive feedback control of intense femtosecond laser pulses, *Optics Express*, **9**(1), 2-6, 2001.
- [85] Takada H, Kakehata M, and Torizuka K, Large-ratio stretch and recompression of sub-10-fs pulses utilizing dispersion managed devices and a spatial light modulator, *Applied Physics B*, **74**, S253-S257, 2002.
- [86] Tearney GJ, Bouma BE, and Fujimoto JG, High-speed phase- and group- delay scanning with a grating-based phase control delay line, *Optics Letters*, **22**(23), 1811-1813, 1997.
- [87] Telenkov SA, Dave DP, and Milner TE, Low-coherence optical probe for non-contact detection of photothermal and photoacoustic phenomena on biomaterials. *Proceedings of AIP*, **657**(1), 852-858, 2003.
- [88] Thomson DJ, Spectrum estimation and harmonic analysis, *Proceedings of the IEEE 0018-9219*, **70**(9), 1055-1096, 1982.

- [89] Vakhtin AB, Kane DJ, Wood WR, Peterson KA, Common-path interferometer for frequency-domain optical coherence tomography. *Applied Optics*, **42**(34), 6953-6958, 2003.
- [90] Vakhtin AB, Peterson KA, Wood WR, Kane, DJ, Differential spectral interferometry: an imaging technique for biomedical applications, *Optics Letters*, **28**(15), 1332-1334, 2003.
- [91] Walden AT, Improved low-frequency decay estimation using the multitaper spectral analysis method, *Geophysical Prospecting*, **38**, 61-86, 1990.
- [92] Walmsley I, Waxer L, Dorrer C, The role of dispersion in ultrafast optics, *Review of Scientific Instruments*, **72**(1), 1-29, 2001.
- [93] Wang H, Zheng Z, Leaird DE, Weiner AM, Dorschner TA, Fijol JJ, Friedman LJ, Nguyen HQ, and Palmaccio LA. 20-fs Pulse shaping with a 512-element phase-only liquid crystal modulator, *IEEE Journal on Selected Topics in Quantum Electronics*, **7**(4), 718-727, 2001.
- [94] Wang SY, Hasty CE, Watson PA, Wicksted JP, Stith RD, and March WF, Analysis of metabolites in aqueous solutions by using laser Raman spectroscopy, *Applied Optics*, **32**(6), 925-929, 1993.
- [95] Weiner AM, Heritage JP, and Kirschner EM, High-resolution femtosecond pulse shaping. *Journal of the Optical Society of America B*, **5**(8), 1563-1572, 1988.
- [96] Wojtkowski M, Srinivasan VJ, Ko TH, Fujimoto JG, Kowalczyk A, and Duker JS, Ultrahigh-resolution, high-speed, Fourier domain optical coherence tomography and methods for dispersion compensation, *Optics Express*, **12**(11), 2404-2422, 2004.
- [97] Wolf E, Determination of the amplitude and the phase of scattered fields by holography, *Journal of the Optical Society of America*, **60**(1), 18-20, 1970.
- [98] Wolf E, Three-dimensional structure determination of semi-transparent objects from holographic data, *Optics Communications*, **1**(4), 153-156, 1969.
- [99] Wollstein G; Schuman JS; Price LL; Aydin A; Stark PC; Hertzmark E; Lai E; Ishikawa H; Mattox C; Fujimoto JG; Paunescu LA, Optical coherence tomography longitudinal evaluation of retinal nerve fiber layer thickness in glaucoma, *Archives of Ophthalmology*, **123**(4), 464-70, 2005.
- [100] Xu Y, Haykin S, Racine RJ, Multiple window time-frequency distribution and coherence of EEG using Slepian sequences and hermite functions, *IEEE Transactions on Biomedical Engineering*, **46**(7), 861-866, 1999.

- [101] Yabushita H, Bouma BE, Houser SL, Aretz HT, Jang I, Schlendorf KH, Kauffman KR, Shishkov M, Kang D, Halpern EF, and Tearney GJ, Characterization of Human Atherosclerosis by Optical Coherence Tomography, *Circulation*, **106**, 1640-1645, 2002.
- [102] Yoon G, Amerov AK, Jeon KJ, and Kim YJ, Determination of glucose concentration in a scattering medium based on selected wavelengths by use of an overtone absorption band, *Applied Optics*, **41**(7), 1469-1475, 2002.
- [103] Yu FTS and Jutamulia S, Spatial light modulators in telecommunication systems. *Proceedings of SPIE*, 4457,164-169, 2001.
- [104] Yun SH, Tearney GJ, de Boer JF, Iftimia N, High-speed optical frequency-domain imaging. *Optics Express*, **11**(22), 2953-2963, 2003.

Vita

Sanghoon Oh was born in Sacheon in Korea, on December 24, 1973, as the second son of Jemmo Oh (吳占模) and Soonhyung Choi (崔順亨). He graduated from Jinju high school in February 1992 and entered the department of Biomedical Engineering in Inje University. During his college, he enlisted in Republic of Korea Air Force (ROKAF) in July 1993. He finished his bachelor's degree in August 1997 and worked at Ergonomics laboratory in Korea Research Institute of Standards and Science (KRISS) for one year. He started his Master's program in Biomedical Engineering graduate program in the University of Texas at Austin in August 1999. After completing his master's degree in 2001, he continued to pursue a Ph.D. degree in the department of Biomedical Engineering in the University of Texas at Austin. Finally he finished all of academic requirements and received Ph.D. degree in May 2006.

Permanent address: 503-13 Chilam-dong
Jinju, 660-280
KOREA (ROK)

This dissertation was typed by the author, Sanghoon Oh.